Atmos. Chem. Phys., 23, 14325–14347, 2023
https://doi.org/10.5194/acp-23-14325-2023

Atmospheric Chemistry and Physics
Open Access
EGU

Understanding greenhouse gas (GHG) column concentrations in Munich using the Weather Research and Forecasting (WRF) model

Xinxu Zhao[1], Jia Chen[1], Julia Marshall[2], Michal Gałkowski[3,4], Stephan Hachinger[5], Florian Dietrich[1], Ankit Shekhar[6], Johannes Gensheimer[1], Adrian Wenzel[1], and Christoph Gerbig[3]

[1]Electrical and Computer Engineering, Technische Unversität München, 80333 Munich, Germany
[2]Deutsches Zentrum für Luft- und Raumfahrt (DLR), Institut für Physik der Atmosphäre, 82234 Weßling, Germany
[3]Airborne trace gas measurements and mesoscale modelling, Max Planck Institute for Biogeochemistry, 07745 Jena, Germany
[4]AGH University of Science and Technology, Faculty of Physics and Applied Computer Science, 30059 Kraków, Poland
[5]Leibniz Supercomputing Centre (LRZ) of the Bavarian Academy of Sciences and Humanities, Boltzmannstr. 1, 85748 Garching, Germany
[6]Department of Environmental Systems Science, ETH Zurich, Universitätstrasse 2, 8092 Zürich, Switzerland

Correspondence: Jia Chen (jia.chen@tum.de)

Received: 13 April 2022 – Discussion started: 17 May 2022
Revised: 27 June 2023 – Accepted: 30 June 2023 – Published: 20 November 2023

Abstract. To address ambitious goals of carbon neutrality set at national and city scales, a number of atmospheric networks have been deployed to monitor greenhouse gas (GHG) concentrations in and around cities. To convert these measurements into estimates of emissions from cities, atmospheric models are used to simulate the transport of various trace gases and help interpret these measurements. We set up a modelling framework using the Weather Research and Forecasting (WRF) model applied at a high spatial resolution (up to 400 m) to simulate the atmospheric transport of GHGs and attempt a preliminary interpretation of the observations provided by the Munich Urban Carbon Column Network (MUCCnet). Building on previous analyses using similar measurements performed within a campaign for the city of Berlin and its surroundings (Zhao et al., 2019), our modelling framework has been improved regarding the initialization of tagged tracers, model settings, and input data. To assess the model performance, we validate the modelled output against two local weather stations and two radiosonde observations, as well as observed column GHG concentrations. The measurements were provided by the measurement campaign that was carried out from 1 to 30 August 2018. The modelled wind matches well with the measurements from the weather stations, with wind speeds slightly overestimated. In general, the model is able to reproduce the measured slant column concentrations of CH_4 and their variability, while for CO_2, a difference in the slant column CO_2 of around 3.7 ppm is found in the model. This can be attributed to the initial and lateral boundary conditions used for the background tracer. Additional mismatches in the diurnal cycle could be explained by an underestimation of nocturnal respiration in the modelled CO_2 biogenic fluxes. The differential column method (DCM) has been applied to cancel out the influence from the background concentrations. We optimize its application by selecting suitable days on which the assumption of the DCM holds true: a relatively uniform air mass travels over the city, passing from an upwind site to a downwind site. In particular, the Stochastic Time-Inverted Lagrangian Transport (STILT) model is used here and driven by our WRF-modelled meteorological fields to obtain footprints (i.e. the potential areas of influence for signals observed at measurement stations), further used for interpreting measurement results. Combining these footprints with local knowledge of emission sources, we find evidence of CH_4 sources near Munich that are missing or

underestimated in the emission inventory used. This demonstrates the potential of this data–model framework to constrain local sources and improve emission inventories.

1 Introduction

Human activities have resulted in an increase of the global average temperature relative to pre-industrial levels of approximately 1.1 °C, a number which is expected to reach around 1.5 °C between 2030 and 2052 (Masson-Delmotte et al., 2018; de Coninck et al., 2018). To achieve the long-term goal of the Paris Agreement to limit temperature increase to 2 °C relative to pre-industrial levels, effective and efficient mitigation at national, regional, and local levels is needed, leading to deep reductions in atmospheric emissions of greenhouse gases (GHGs) over the coming decades (Masson-Delmotte et al., 2021). More than half of the world's population resides in urban areas, which are directly responsible for over 30 % of the global GHG emissions (Masson-Delmotte et al., 2018) and approximately 65 % of global energy use (IRENA, 2016). Thus, cities play a vital role in addressing the challenge of carbon mitigation. The development of science-based methods to estimate carbon emissions from urban areas is crucial for developing effective and coherent adaptation actions and monitoring their success.

As the continent with the highest population density, Europe plays a major role in future mitigation efforts. In recognition of this fact, the European Commission aims to make Europe climate neutral by 2050 (EU Commission, 2018). Furthermore, member countries of the European Union (EU) have also adopted individual strategies consistent with that goal. For example, the German government plans to reduce national GHG emissions by more than 65 % compared to 1990 by 2030, achieving climate neutrality by 2045. Local-scale initiatives have also been put in place. Munich, currently the third largest city in Germany with over 1.5 million inhabitants, has set an even more ambitious goal, aiming to be climate neutral by 2035.

To confront the challenge of carbon mitigation in cities and reach the goals set by individual municipalities, a multitude of urban atmospheric networks have been built worldwide to optimize urban emissions (DeCola et al., 2018). Using the measurements they provide, GHG concentrations can thus be monitored in and around cities, and more accurate emission estimates can be derived, interpreting these measurements with atmospheric transport modelling and statistical techniques (Lauvaux et al., 2016; Staufer et al., 2016). Based on these quantitative assessments, more reliable scientific guidance can be provided to policymakers in order to plan local emission reductions effectively and monitor mitigation efforts.

Two standard approaches are widely used for estimating emission fluxes: the bottom-up approach and the top-down approach. Using the bottom-up approach, the total fluxes are estimated on the basis of statistical activity data from individual sectors (e.g. power plants, traffic) and the corresponding emission factors. This approach is widely used for generating global and national sector-by-sector emission inventories, for example, the Emissions Database for Global Atmospheric Research (EDGAR; Janssens-Maenhout et al., 2019). The emissions produced using this technique are often quite uncertain, owing to missing or simplified knowledge of emission processes and the considerable heterogeneity in space and time (Klausner et al., 2020). By using the top-down approach, estimated emission fluxes can be refined using additional information provided by measurements of atmospheric concentrations. Prior emission estimates, usually estimated by the bottom-up approach, are used as inputs for an atmospheric transport model, and the resultant concentrations are compared to the atmospheric composition measurements (Zhao et al., 2019; Shekhar et al., 2020). The emission estimates can then be optimized using either a mass-balance approach (Heimburger et al., 2017) or other inverse techniques (Jones et al., 2021). In terms of GHG emission estimation for cities or an area of interest, the top-down inversion approach has frequently been applied in modelling studies accompanied by urban measurement networks, for example, in California (Turner et al., 2016), Paris (Staufer et al., 2016), Boston (Sargent et al., 2018), Berlin (Klausner et al., 2020), and Indianapolis (Jones et al., 2021). Inversion models still show considerable potential for improvement, owing to limited knowledge about the characteristics and spatial distribution of emission sources (e.g. missing or underestimated sources, inner-city traffic), uncertainties in background concentrations, and the difficulty of modelling transport in complex urban environments, thus representing the observations. Furthermore, emissions that are highly heterogeneous in time and space are challenging from the perspective of both measurements and modelling and demand extra care in their interpretation (e.g. Vaughn et al., 2018).

To aid in reaching the goal of climate neutrality and track emissions in Munich, our group has established a novel automated urban sensor network (MUCCnet; Munich Urban Carbon Column Network, accessible via https://atmosphere.ei.tum.de/, last access: 10 September 2023; Dietrich et al., 2021) for continuous, long-term monitoring of GHGs in and around Munich. In brief, MUCCnet takes measurements simultaneously at five locations to capture concentration signals in and around the city, with the goal of estimating city emissions using continuous measurements accompanied by

atmospheric models. MUCCnet is designed with the differential column method (DCM; Chen et al., 2016) in mind, developed to quantify the emissions within a certain area, for example, a single city. This is done by capturing concentration enhancements between downwind and upwind sites, so that a signal can be attributed to the emissions from the area in between. Several studies have used this approach combined with atmospheric models to study urban and local emissions, for example, in Berlin (Hase et al., 2015; Zhao et al., 2019); Paris (Vogel et al., 2019); Munich (Toja-Silva et al., 2017); and Chino, California (Chen et al., 2016; Viatte et al., 2017). Detailed descriptions of MUCCnet and its measurement principle are presented in Sect. 4.1 and Dietrich et al. (2021).

On the basis of MUCCnet measurements and our previous study that interpreted data from a measurement campaign around Berlin (Hase et al., 2015; Zhao et al., 2019), we have set up a modelling framework for Munich. This is based on the Weather Research and Forecasting model (WRF) enhanced with a biospheric flux module (WRF-GHG; Beck et al., 2012), which runs at a horizontal resolution of up to 400 m over the city. WRF is a mesoscale model commonly used for weather and atmospheric studies, and WRF-Chem has been extended with additional modules for tracer transport and chemistry (now including the GHG modules; Skamarock et al., 2008). With WRF-Chem (Peckham et al., 2017), modelled meteorological fields are used to drive simulations of the atmospheric transport of trace gases, for example, GHGs (Zhao et al., 2019) and air pollutants (Georgiou et al., 2018). Our model for Munich aims to reproduce observations from the five measurement locations in MUCCnet so as to aid in their interpretation and better understand the processes driving the emission and uptake of GHGs around the city. Apart from generating concentration fields for different emission tracers, the output from the modelling system will be further used as input for other studies. For instance, highly resolved meteorological fields can drive particle transport models (Fasoli et al., 2018). These Lagrangian footprints can then be used for inversion studies, similar to Heerah et al. (2021), who optimized dairy CH_4 emissions across the San Joaquin Valley using WRF coupled with Stochastic Time-Inverted Lagrangian Transport model (WRF-STILT) inversions. Currently, an adapted Bayesian inversion model based on Jones et al. (2021) is being developed to infer anthropogenic CO_2 emissions, with the consideration of biogenic fluxes.

In this paper, we describe our model framework in detail and apply it in the interpretation of the observations collected by MUCCnet from 1 to 30 August 2018. Compared to the previous study in Berlin (Zhao et al., 2019), the model has been updated, and several aspects related to model settings and initialization processes have been improved. As an example, more precise anthropogenic fluxes have been used for the tagged emission tracers. All these model-related aspects are described in Sect. 2. In Sect. 3, we assess the performance of our model by comparing its output to the measurements from two local weather stations. A model–measurement comparison of GHG column concentrations is presented in Sect. 4. In Sect. 5, we optimize the application of DCM and use it to assess the model performance and further track missing or underestimated emission sources around MUCCnet, through combining footprints generated by the particle transport model STILT (Fasoli et al., 2018) and the knowledge of local sources.

2 Modelling framework description

We use WRF-Chem Version 3.9.1.1 (Skamarock et al., 2008; Peckham et al., 2017) with an updated GHG module (Beck et al., 2012) in order to simulate the fluxes and transport processes of atmospheric GHGs in and around Munich at a horizontal resolution of up to 400 m. The main component of the setup is the WRF-ARW model, based on the fully compressible non-hydrostatic Euler equations (Skamarock et al., 2008). We take realistic meteorological driving data from the ERA5 reanalysis (Hersbach et al., 2020), extracted at approximately 31 km horizontal resolution and with 137 vertical levels from ground level to 0.01 hPa. These data provide the initial and boundary conditions for the meteorological fields.

In our model, biogenic fluxes of GHGs are simulated online, driven by meteorological parameters at native model resolution, in addition to other inputs. Furthermore, fluxes from external emission inventories are included as inputs, and these surface fluxes are transported as passive tracers in WRF (Beck et al., 2012). Compared to the originally developed WRF-GHG, in which the GHG modules had to be explicitly integrated with WRF Version 3.2 (see Zhao et al., 2019), these modules have been added to the official WRF-Chem repository since WRF-Chem Version 3.4. It is worth noting that the GHG module does not take into account atmospheric chemical reactions (as it treats GHGs as passive tracers). This is, however, not expected to produce significant biases, owing to the long lifetimes of GHGs compared to the relatively short residence time of tracers in the regional domain (Super et al., 2017; Dekker et al., 2017).

The model is configured in a three-domain nested configuration, with horizontal resolutions of 10 km for the outermost domain (D01), 2 km for the intermediate domain (D02), and 400 m for the innermost domain (D03), as illustrated in Fig. 1. The spatial grids are assigned using the Lambert conformal conic (LCC) projection. The simulations are carried out with model integration time steps of 30, 6, and 1.2 s for each domain, with model outputs saved at time intervals of 3 h, 1 h, and 15 min, respectively. We define 46 vertical levels from the surface up to 50 hPa, 21 of which are in the lowest 1 km of the atmosphere. All five total column measurement sites from MUCCnet are located inside D03. The Mellor–Yamada–Janjić (MYJ) planetary boundary layer (PBL) parameterization scheme is employed to resolve mod-

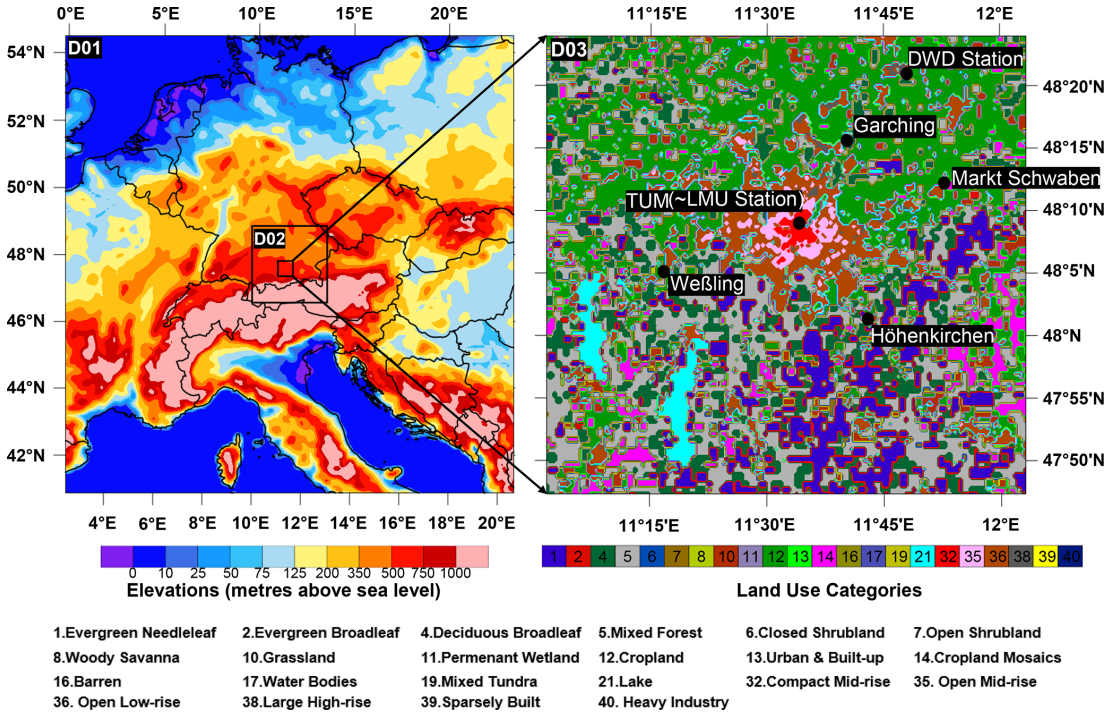

Figure 1. Topography map for the entire domain area (left panel). The right panel shows the land-use classification in D03, including the 16 International Geosphere-Biosphere Programme (IGBP)-modified MODIS land-cover types (from 1 to 21, as illustrated in the colour bar and labels), and 6 classified LCZ land-cover categories defined for the urban areas of D03 (numbers larger than 30, as illustrated in the colour bar and labels). The five measurement sites in our MUCCnet campaign and the surface weather stations used for the model–measurement comparison of meteorological fields are marked as black dots on the right panel. The national boundaries and coastlines in the left panel are from National Center for Atmospheric Research (NCAR) Graphics Version 4.1 (© UCAR/NCAR).

elled vertical turbulent mixing and accurately depict meteorology conditions (Hu et al., 2010).

To better capture the urban landscape features and improve the urban model performance (Ching et al., 2018; Mughal, 2020), extra urban land-use–land-cover categories are provided for the innermost domain (D03, area of Munich), which enables us to use the urban canopy multi-layer scheme in WRF (Brousse et al., 2016). This is done by reclassifying the land-cover categories for urban areas, while keeping the other land-cover categories unmodified. The recategorized land-cover types are derived from the European Local Climate Zone (LCZ) map (Demuzere et al., 2019), extracted for our high-resolution domain (Fig. 1). More information regarding this procedure can be found in Sect. S3 of the Supplement.

The initial and lateral boundary conditions in the simulated background concentration fields of CO_2 and CH_4 are taken from the Integrated Forecasting System (IFS) Cycle 45r1, implemented by ECMWF, at a horizontal resolution of approximately 40 km (Rémy et al., 2019; Browne et al., 2019) The IFS Cycle 45rl is operated by the European Centre for Medium-Range Weather Forecasts (ECMWF) as part of the Copernicus Atmosphere Monitoring Service (CAMS). IFS Cycle 45rl is referred to as CAMS for simplicity.

Biogenic CO_2 fluxes are implemented online utilizing the Vegetation Photosynthesis and Respiration Model (VPRM; Mahadevan et al., 2008; Chen et al., 2020), a simple diagnostic light-use-efficiency (LUE) model coupled to WRF-Chem. VPRM does not reproduce the physiological processes of vegetation but rather calculates gross primary production (GPP) using the input of meteorological variables and vegetation indices derived from remote sensing data. Ecosystem respiration (RES) is estimated using a simple linear model related to the air temperature and vegetation-specific parameters. Finally, the hourly CO_2 net ecosystem exchange (NEE) is the difference between GPP and RES. In detail, the entire calculation is based on satellite-derived indices, short-wave radiation, and surface temperature at 2 m above the ground level as simulated by WRF (Beck et al., 2012). The indices (i.e. Enhanced Vegetation Index (EVI) and Land Surface Water Index (LSWI)) here are derived from reflectance data measured by MODIS, specifically the product MOD09A1 Version 6. MODIS has resolutions of 0.5–1 km depending on the wavelength band and a temporal resolution of 8 d (Vermote, 2015). The MODIS reflectance data are aggregated and interpolated onto the LCC projection, and the vegetation is classified following the SynerCover Product (SYNMAP) data with a resolution of 1 km (Jung et al., 2006).

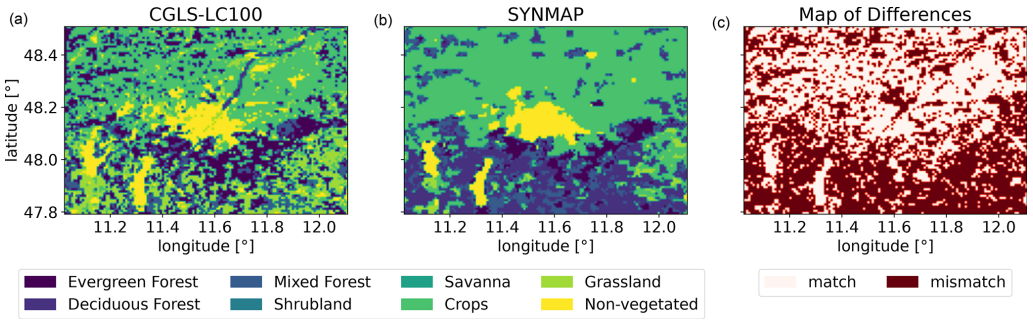

Figure 2. The maps of the vegetation classification **(a)** with and **(b)** without refining using CGLS-LC100 and their difference **(c)**.

Because the 1 km resolution of the SYNMAP dataset is unable to resolve vegetation within cities, urban areas are essentially masked out, and VPRM does not produce any fluxes within cities (see the middle panel in Fig. 2). Thus, we extend and refine the vegetation classification using the Dynamic Land Cover map of the Copernicus Global Land Service at a resolution of 100 m (CGLS-LC100). This refined classification is used for our innermost domain to better capture the urban biogenic signals of CO_2. A comparative visualization of the vegetation classification maps with and without the refinement around Munich is shown in Fig. 2. Details of this reclassification are described in Table S1 of the Supplement.

CH_4 fluxes from wetlands are estimated using the Kaplan model (Kaplan et al., 2006), which is run online within WRF-Chem. This model calculates CH_4 emissions from anaerobic microbial production in wetlands as a fraction of heterotrophic respiration (Beck et al., 2013). The flux estimates depend on the modelled soil moisture, soil temperature, and carbon pool from the Lund–Potsdam–Jena model, which is used for classifying the wetland fractions in the domain (Beck et al., 2012).

The first version of the GHG and co-emitted species emission database produced by the Netherlands Organisation for Applied Scientific Research (TNO; dataset TNO_GHGco_v1.1; Super et al., 2020) is used to initialize anthropogenic fluxes as tagged tracers. This dataset provides annual gridded anthropogenic emissions for 2015 at a horizontal resolution of $0.05° \times 0.1°$ (latitude $\times$ longitude, approximately 6 km $\times$ 6 km), covering most of Europe and part of northern Africa. In addition to the gridded emissions, point emission sources (e.g. power plants) are reported separately with geographical coordinates. These emissions are classified into 14 sectors, following the Gridding Nomenclature for Reporting (GNFR) emission categories (A to L), i.e. industry, public power, road transport, and other anthropogenic sources. Furthermore, a high-resolution version of TNO_GHGco_v1.1, at a resolution of $1/120° \times 1/60°$ (latitude $\times$ longitude, approximately 1 km $\times$ 1 km; van der Gon et al., 2019), is available for central Europe (i.e. all of Germany and parts of France, Poland, and the Netherlands, etc.). This version of TNO_GHGco_v1.1 was prepared to support model studies at the local scale in the CO_2 Human Emissions project (CHE; van der Gon et al., 2019). Since our outermost domain is not fully covered by the high-resolution version of TNO_GHGco_v1.1, we use the lower-resolution (6 km) emissions for the outermost domain (D01) and the high-resolution version for the other two domains (D02 and D03 in Fig. 1). To prepare the input for WRF-Chem, the required temporal disaggregation of the annual emissions was performed based on time-dependent scaling factors for monthly, weekly, and diurnal variations (Zhao et al., 2019; Super et al., 2020). In addition, we release the emission fluxes from the point sources in TNO_GHGco_v1.1 from different heights above the ground, using the vertical profiles provided in Table 2 of Brunner et al. (2019). The reallocation of point sources to vertical levels in our domain is illustrated in Fig. S2 of the Supplement.

3 Model–measurement comparison for wind fields

To assess the performance of our model framework and evaluate the modelled meteorological variables used for transporting the fluxes, some key meteorological parameters are compared to measured values provided by two local weather stations and two radiosonde observations.

3.1 Comparison for surface wind fields

The first station is located at the Meteorological Institute of the Ludwig Maximilian University of Munich (LMU; latitude: 48.15°, longitude: 11.57°, altitude: 561 m), close to the centre site of MUCCnet. This station can provide time series of meteorological variables second by second. We compare the model to five meteorological variables measured at LMU: the temperatures at heights of 2 and 30 m above the ground ($T2$ and $T30$), the precipitation, and the wind speed and direction at 30 m above the ground (WS30 and WD30). The other station we consider is operated by the German Meteorological Service (Deutscher Wetterdienst in German, DWD). This automated weather station is located at Munich airport and has station ID 01262 (latitude: 48.35°, longitude: 11.81°, altitude: 446 m). We use the following variables mea-

sured at the airport for comparison with our model: $T2$, precipitation, relative humidity, air pressure, and the wind speed and direction at 10 m above the ground (WS10 and WD10).

As one of the key drivers for the transport of trace gases in the model, the simulated wind field directly impacts the transport patterns of the tracers. Thus, it is particularly important to assess the model performance with regards to the wind field. Here, we employ the measured WS30 and WD30 at the LMU station and WS10 and WD10 at the DWD station. The LMU station measures the winds every second, while the wind data given by DWD are recorded as 10 min means. We apply a cut-off wind speed threshold ($0.5\,m\,s^{-1}$ in our case) to the values shown in Fig. 3, owing to large uncertainties in wind directions during low wind speed periods (Zhao et al., 2019).

A comparison between the modelled and measured winds at the LMU station is shown in Fig. 3. Prevailing wind directions both in the simulations and measurements are either easterly or westerly during the daytime, while the prevailing winds at night are generally from the southwest. The measurements (Fig. 3a.1, a.3 and a.5) show larger scatter in the wind direction over August compared to the simulations. The evaluation of wind directions is treated following the method presented in Jiménez and Dudhia (2013). Along the time series, the simulated (Fig. 3b: red crosses) and measured (blue dots) wind speeds show similar variability, but the model generally overestimates wind speeds, with a root mean squared error (RMSE) of $2.0\,m\,s^{-1}$ and a mean absolute error (MAE) of $1.2\,m\,s^{-1}$. During the measurement periods (see Sect. 4), shown by the grey shaded areas in Fig. 3b, the model performs better, with a RMSE of $1.6\,m\,s^{-1}$ and a MAE of $1.1\,m\,s^{-1}$. Regarding a comparison of the wind directions between the model and measurements (see Fig. 3c), the model mostly follows the measured fluctuations of wind directions but with some difference over time (RMSE = 64.1° and MAE = 56.1°). The model performance is reduced in some periods, for example, between 24 and 26 August, when the variability of the wind direction is remarkably lower in the model. Over the measurement periods marked by grey areas, smaller differences between the WRF and the in situ surface wind directions are found, with a RMSE of 58.2° and MAE of 51.8°.

In addition to this model–measurement comparison for WS30 and WD30, similar comparisons regarding the other meteorological variables have also been performed and are presented in Sect. S5 of the Supplement. These comparisons indicate that our model has the capability to provide reasonable simulated meteorological fields for driving the transport of trace gases.

3.2 Comparison for vertical wind profiles

In order to assess whether the WRF meteorological fields allow the transport model (STILT; Fasoli et al., 2018) to produce realistic footprints (see Sect. 5.2), we have evaluated our modelled height-dependent wind fields using observations. This assesses their accuracy in the vertical dimension more deeply than the comparisons of the surface wind fields shown in Sect. 3.1.

Figure 4 shows modelled and measured wind speed and direction profiles for 16 and 22 August. The comparison uses radiosonde data from two sites (Altenstadt and Hohenpeißenberg, marked as black squares in Fig. 9b), provided by Integrated Global Radiosonde Archive (IGRA). This archive collects radiosonde and pilot balloon observations along significant vertical levels historically and in near-real-time from around 800 distributed stations worldwide (Durre et al., 2018). On both days at Altenstadt (Fig. 4a and b), the model reproduces the observed winds well, especially at noon, while outliers in wind direction always exist at the lowest level in the morning, and some mismatches appear at 18:00 UTC. Regarding the wind profiles measured at Hohenpeißenberg, the modelled wind directions at higher altitudes agree quite well with the observations, with mismatches close to the ground level. It is worth noting that our domain is close to the Alps, with complex topography making meteorological modelling more challenging. The results need to be interpreted in this context.

4 Model–measurement comparison for concentration fields and model tracer analysis

This part of our study is dedicated to a comparison of the measurements from MUCCnet to column concentrations for different tagged tracers extracted from the simulation output fields. Section 4.1 contains relevant information on the measurements used for interpreting the model, and the model–measurement comparison is discussed in Sect. 4.2. The final section (Sect. 4.3) characterizes changes in concentrations caused by individual anthropogenic emission processes, as represented by our model.

4.1 Description of MUCCnet and the measurement campaign

Our WRF model framework for Munich is designed to study GHG concentrations in connection with the Munich Urban Carbon Column network (MUCCnet; Dietrich et al., 2021). In MUCCnet, five compact Fourier transform infrared (FTIR) spectrometers (EM27/SUN by Bruker Optics) have been deployed, four of which were located around Munich at a radius of 20 km for the 2018 period analysed in this study (this was later changed to 10 km in 2019). The fifth instrument has been set up close to the centre of Munich, at the TUM campus (see Fig. 1). By using the sun as a light source, the EM27/SUN measures near-infrared solar spectra (Gisi et al., 2012). In MUCCnet, the recorded interferograms are automatically transformed to spectra, converted to column-averaged dry-air mole fractions (DMFs) of CO_2 and CH_4 between the instrument and the end of the atmosphere in the

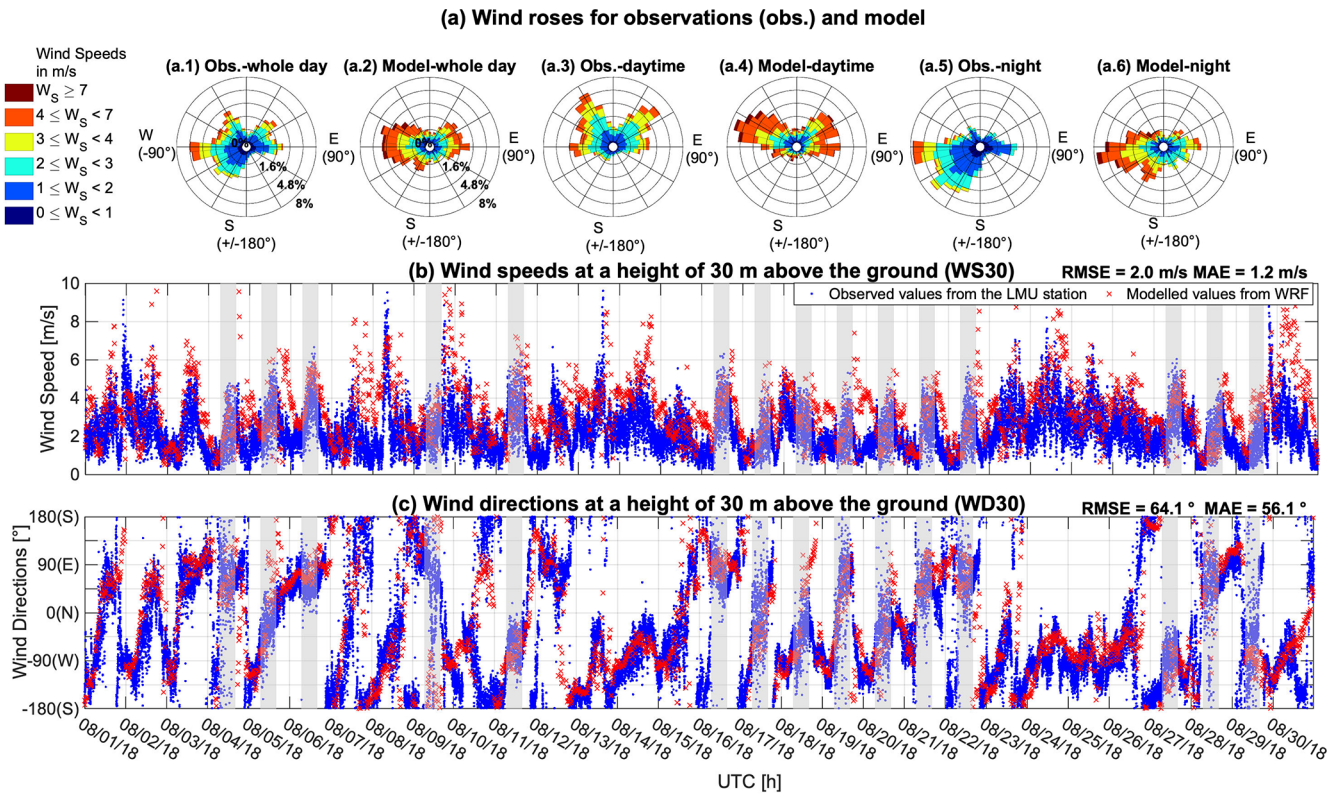

Figure 3. Wind roses **(a)** and time series of simulated and observed wind speeds **(b)** and wind directions **(c)** at a height of 30 m above the ground at LMU. Wind roses for the measurements over August 2018 are plotted in panels **(a.1)** for 24 h **(a.3)**, for daytime from 06:00 to 17:00 UTC only, and, **(a.5)** for night-time only, while panels **(a.2)** and **(a.4)**, and **(a.6)** represent the modelled values. Each wind rose indicates WS30, WD30, and the frequency (% scale) of wind coming from a particular direction during the targeted period. The blue dots in panels **(b)** and **(c)** represent the measured values from the LMU station and the red crosses represent the simulation. The grey shaded areas mark the measurement periods used for the model–measurement comparison of column concentrations in Sect. 4.

direction towards the sun, and further uploaded to the official website of MUCCnet (https://atmosphere.ei.tum.de). The retrieval algorithm GFIT GGG-2014 (Wunch et al., 2015) was applied during the measurement campaign of 2018, while currently, MUCCnet is using the PROFFIT (Hase et al., 2004; Frey et al., 2015, 2019; Alberti et al., 2022) and GGG-2020 algorithms (Laughner et al., 2023). Additionally, the hydrogen fluoride (HF) correction (Saad et al., 2014) is not applied in our retrieval process of CH_4. All five instruments are automatically operated and controlled using our universal enclosure systems and two software programs (Heinle and Chen, 2018; Dietrich et al., 2021). Detailed information on the EM27/SUN instrument can be found, for example, in Hedelius et al. (2016), Chen et al. (2016), Hase et al. (2016), and Frey et al. (2019).

In this study, we compare simulations to measurements collected during a campaign that was carried out from 1 to 30 August 2018 (Dietrich et al., 2019, 2023). Table S4 in the Supplement shows relevant parameters for assessing the measurement performance during that period, including the number of observations per day for each site and the ground-level wind information for each day, i.e. the daily mean of WS30 and the approximate change in WD30 during the day, provided by the LMU station.

The EM27/SUN measures column-averaged DMFs of CO_2 and CH_4, hereafter referred to as XCO_2 and XCH_4. Over the entire campaign period in 2018, the mean of the measured XCO_2 for all five sites is 404.4 ppm with a standard deviation of 1.2 ppm, ranging from 400.8 to 408.1 ppm. For XCH_4, the measurements range from 1840.5 to 1896.0 ppb, with a mean of 1865.5 ppb and a standard deviation of 9.1 ppb. Since the operation of the instruments is strongly influenced by weather conditions, the spatial and temporal measurement coverage for some days (e.g. 1–3 August) is limited (see Table S4). By assessing the main characteristics of the measurement days during the campaign, we selected 15 d in total with good measurement conditions (i.e. with a quality level better than "++"; see Table S4 and Sect. S6 of the Supplement) to make the model–measurement comparison: 4–6, 9, 11, 16–22 and 27–29 August 2018. Details of the campaign and side-by-side calibrations are discussed in Sects. 4.1 and 5 of Dietrich et al. (2021).

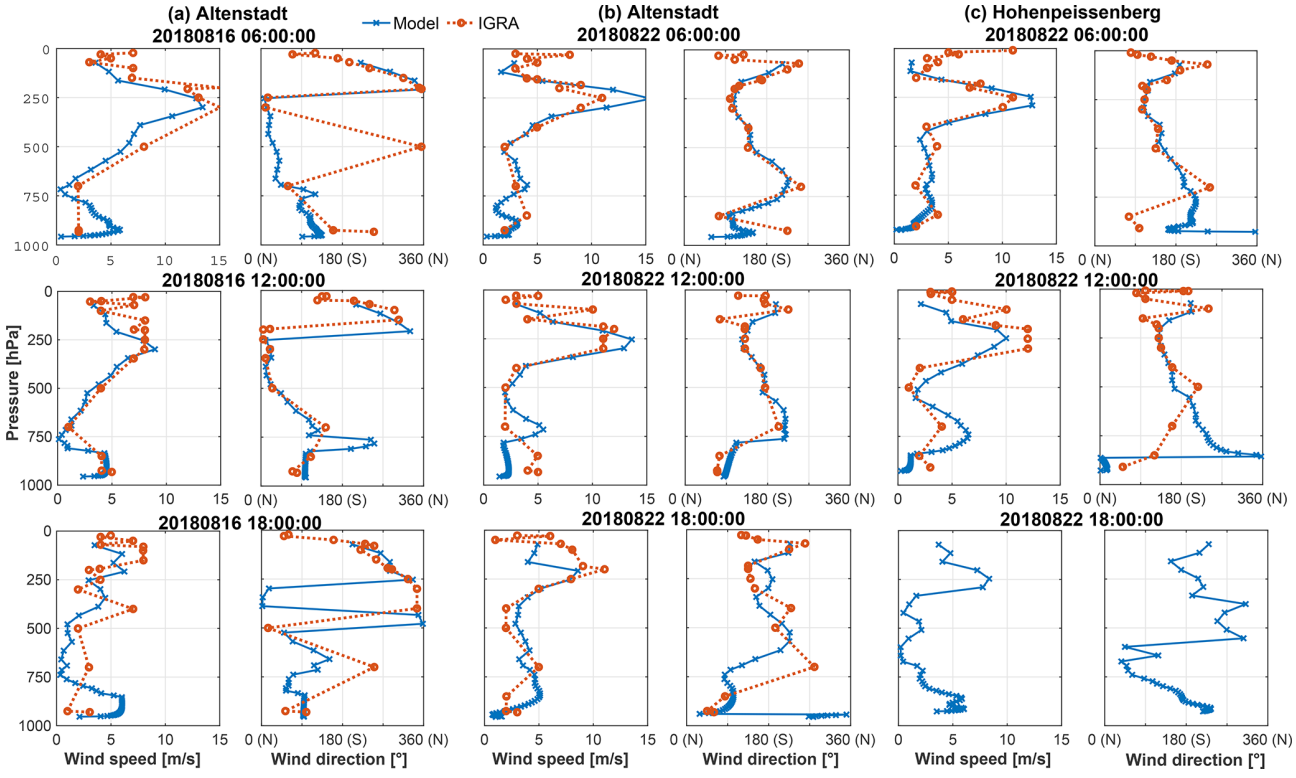

Figure 4. Wind profile comparison between the model (dashed orange line) and the measurements (solid blue line) from two radiosonde locations, i.e. **(a, b)** Altenstadt on 16 and 22 August and **(c)** Hohenpeißenberg on 22 August. Measurements are lacking in the IGRA at 18:00 UTC on 22 August.

4.2 Model–measurement comparison of XCO_2 and XCH_4

In our modelling framework, the anthropogenic emission fluxes from an inventory (TNO-GHGco; see Sect. 2 for details) are used as fluxes for tagged tracers, each representing a source category group available in the inventory (Super et al., 2020). These tracers are transported passively throughout the model domains using internal WRF-Chem transport schemes. Then, the total concentrations for a trace gas are derived by summing up the contributions from individual emission processes (i.e. the different tagged tracers) and the background concentrations for this gas, provided by CAMS and advected from the model boundaries as a separate tracer.

4.2.1 Calculation of smoothed slant column concentrations

The modelled vertical concentration profiles are converted to pressure-weighted column-averaged concentrations. That is to say, for the trace gas G, the simulated column concentration at a specific location and time $XG(x, y, t)$ can be calculated as follows:

$$XG(x,y,t) = \sum_{l=1}^{L_{\text{ver}}} \left[w_l(x,y,t) \times G_l(x,y,t) \right], \tag{1}$$

where G_l stands for the simulated mole fraction at the location (x, y) and time t at the lth vertical layer of WRF. L_{ver} is the total number of the vertical layers (i.e. 45 in our study), and w_l is the weight of the lth vertical layer, which can be obtained as

$$w_l(x,y,t) = \frac{\Delta P_l(x,y,t)}{P_{\text{sf}}(x,y,t) - P_{\text{tp}}}, \tag{2}$$

where P_{tp} is the hydrostatic pressure at the top of the model (i.e. 50 hPa), and P_{sf} is the surface pressure. ΔP_l denotes the pressure difference between the top and the bottom of the lth vertical layer. Here we use the WRF-meteorology-derived pressure profiles to calculate the weights for each vertical layer, instead of the pressure profiles used for EM27 retrievals (NCEP). This is convenient, as the WRF-modelled profiles for both pressure and concentrations have the same vertical structure, and no interpolation is necessary. Furthermore, only slight differences in pressure at higher altitudes were found between the WRF model and NCEP (see Sect. S10).

However, when comparing our modelled values to the measurements here, we need to consider the characteristics of the instruments in a more accurate way. The EM27/SUN records the spectra along a slant column from the sun to the ground, instead of a vertical column perpendicular to

the ground. Simulated concentration fields of CO_2 and CH_4 used for the model–measurement comparison in this study must therefore be aggregated along the slant columns from the ground to the sun during the period of the available measurement dates.

In addition, when reconstructing the vertical structure of the atmosphere during the retrieval process of ground-based remote sensing instruments (e.g. Vogel et al., 2019; Zhao et al., 2019) and satellites (e.g. Ohyama et al., 2020), an averaging kernel (AK) is used to represent the altitude-dependent column sensitivity (Borsdorff et al., 2014). For solar-viewing instruments, its shape is strongly dependent on the solar zenith angle (SZA). The retrieved quantity then typically depends considerably on the AK as well as on the a priori profile used in the retrieval. Accordingly, when the modelled values are compared to such measurements, they also need to be smoothed using the AK and the a priori profile in order for the comparison to be valid. Since the EM27/SUN has a spectral resolution of only $0.5\,\mathrm{cm}^{-1}$, we can use a fitted AK matrix, which is obtained by applying a simple least-squares fit to a given a priori AK profile. The details related to applying the AK to the model data were previously described in detail in Sect. 3.3 of Zhao et al. (2019).

Thus, the simulations are mostly interpreted by comparing the aggregated and AK-smoothed modelled values to column measurements. The smoothed slant column concentration for a target gas XG^{S}_{sla} is calculated following Eq. (3) (see Vogel et al., 2019; Zhao et al., 2019):

$$XG^{S}_{sla}(x,y,t) = \sum_{l=1}^{L_{ver}} w_{sla,l}(x,y,t) \times \left[AK_{G,l}(t) \times G_{sla,l}(x,y,t) + (1 - AK_{G,l}(t)) \times G_{pri,l}\right], \quad (3)$$

where $G_{sla,l}$ denotes modelled concentrations for trace gas G at the lth vertical layer following the slant column along the line of the sun, $AK_{G,l}$ is the fitted AK of the gas G at the lth vertical layer and time t, $G_{pri,l}$ stands for the mixing ratio of the a priori profile for trace gas G at the lth vertical layer, and $w_{sla,l}$ is the weight of the lth vertical layer along the slant column. We have used the a priori profile from the Whole Atmosphere Community Climate Model (WACCM) Version 6 for 2018.

It should also be noted here that the measured samples are filtered during the autonomous retrieval process in MUCCnet (Dietrich et al., 2021). Specifically, to reduce uncertainties caused by high air masses, measurements are discarded when they are observed at SZA larger than 75° (Tu et al., 2020; Gisi et al., 2012). Thus, the measurement period each day ranges from around 06:00 to 17:00 UTC and lasts for approximately 11 h in summer. When comparing the simulations to the measurements, the simulated CO_2 and CH_4 concentration profiles along the slant column during the period of the available measurement dates are aggregated to the AK-smoothed column concentrations ($XCO^{S}_{2,sla}$ and $XCH^{S}_{4,sla}$) by using Eq. (3). In the following figures, the grey shaded areas are used to mark these measurement periods used for the model–measurement comparisons.

4.2.2 Comparison of daily mean concentrations and estimation of CO_2 mean bias

The daily mean measured and modelled values ($XCO^{S}_{2,sla}$ and $XCH^{S}_{4,sla}$) for the 15 studied days and their scatter plots are shown in Fig. 5. When producing daily-averaged modelled values, we have considered the limited measurement period on each day, that is, from around 06:00 to 17:00 UTC. For CO_2, the simulated smoothed column concentrations ($XCO^{S}_{2,sla}$, dotted lines in Fig. 5a) are overall overestimated compared to the measurements, with a mean bias (MB) of 3.7 ± 0.9 ppm, the latter value giving the standard deviation of the MB over all measurement days. This bias for $XCO^{S}_{2,sla}$ is mainly attributed to the initial and boundary conditions of the concentration fields in the model as provided by CAMS, which has also been seen in other studies. A discussion of the XCO_2 bias is included in Sect. S14 of the Supplement. Gałkowski et al. (2021) found a similar bias between the CAMS product and airborne measurements in the free troposphere over Europe, with a MB of 3.7 ± 1.5 ppm, which they have attributed to the far-field contributions to the local signal. While the agreement between the biases reported in their study and here is excellent, it should be noted that the numbers are not fully comparable, as the authors of the quoted study evaluated a limited section of the vertical column (namely between 3–10 km a.m.s.l.) using in situ data, thus excluding the lower tropospheric (below 3 km) and the stratospheric components of the total column. Moreover, Tu et al. (2020) also reported a bias when comparing CAMS to their column measurements from the Collaborative Carbon Column Observing Network (COCCON) site at Kiruna, Sweden, with a MB of 3.7 ± 1.8 ppm.

As can be seen in the scatter plot of $XCO^{S}_{2,sla}$ (Fig. 5b), the measurements generally exhibit more scatter (seen in the magnitude of the error bars in the x direction) compared to the simulation (the error bars in the y direction), and the slope of the linear regression is only 0.45. The smaller standard deviations in the model represent weaker fluctuations over the daily mean. This will be discussed further in Sect. 4.2.3 when looking into the model–measurement comparison at higher temporal resolutions.

Figure 5c and d show that the daily mean modelled values of $XCH^{S}_{4,sla}$ (solid lines in Fig. 5c) agree well with the daily mean measurements. The model is able to capture most of the variations in the daily mean values, while in general the observed values are slightly higher, with a linear regression slope of 0.73 and a negative MB (-1.8 ± 4.0 ppb). This small bias could be caused by the initial and lateral boundary conditions from CAMS or be due to unknown or underestimated emissions. Comparing CH_4 in the CAMS product with in situ observations in the troposphere, Gałkowski et al. (2021) also

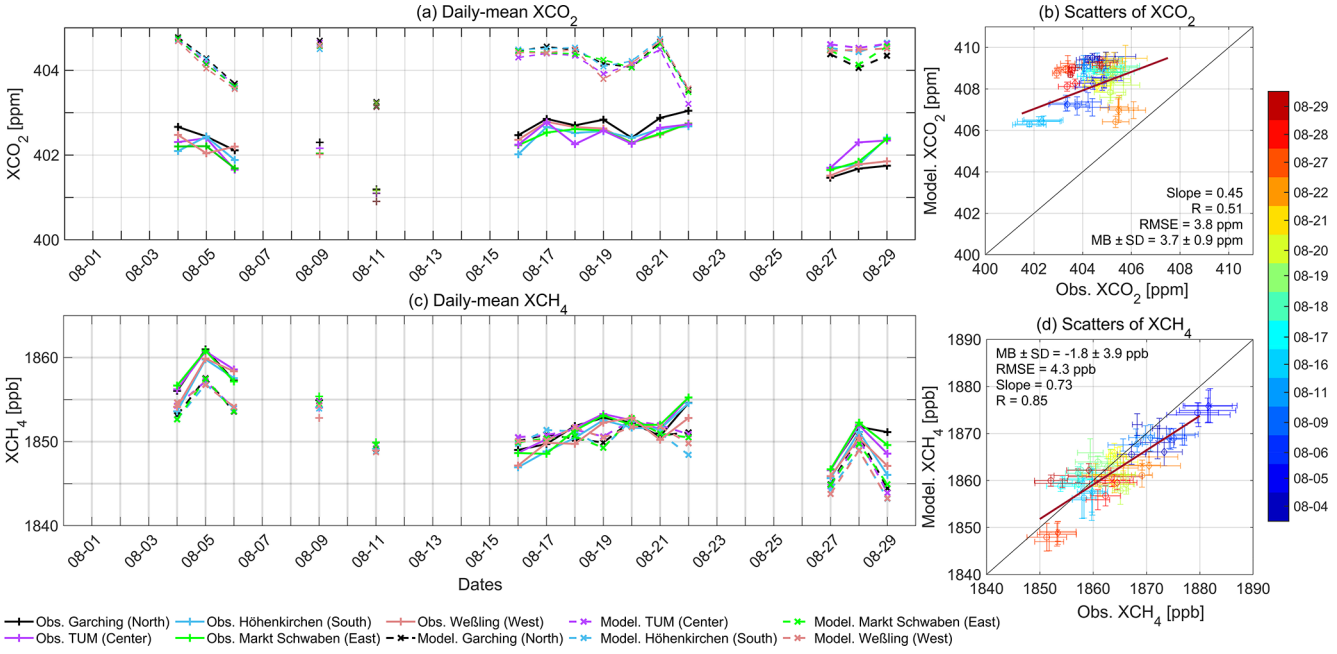

Figure 5. Time series and scatter plots for XCO_2 **(a, b)** and XCH_4 **(c, d)**. In panels **(a)** and **(c)**, the dashed lines represent the daily mean modelled $XCO^S_{2,sla}$ and $XCH^S_{4,sla}$, while the solid lines denote the measurements. Colours in panels **(a)** and **(c)** mark the different measurement sites. In scatter plots **(b)** and **(d)**, colours represent the values for different measurement days, as marked in the colour bar. The error bar represents the standard deviation of the measured and simulated values at each site.

reported a negligible MB but a relatively large standard deviation (0 ± 14 ppb) in their setup.

4.2.3 Comparison between model and measurements: intra-day concentrations

In order to obtain a more detailed view on how the model behaves at higher temporal resolution, the longest stretch of consecutive measurements in the campaign (i.e. from 16 to 22 August) is analysed here. Figures 6 and 7 show the daily curves of $XCO^S_{2,sla}$ and $XCH^S_{4,sla}$ at five sites for these 7 consecutive days against the corresponding modelled values with hourly temporal resolution. Model–measurement comparisons for the rest of the days are shown in Figs. S5 and S6 of the Supplement.

Due to the restriction of SZAs and the corresponding availability of measured values provided by the MUCCnet (see Sect. 4.1), these model–measurement comparisons of the total column concentrations for GHGs can only be made during the daytime, from approx. 06:00 to 17:00 UTC (see Fig. 6). As mentioned in Sect. 4.2.1, the modelled and observed slant column concentrations ($XCO^S_{2,sla}$ and $XCH^S_{4,sla}$) used for the model–measurement comparisons are smoothed using the SZA-dependent AK based on Eq. (3). Figures 6 and 7 also illustrate the contributions to the total column concentrations of CO_2 and CH_4 (XCO_2 and XCH_4) from different tracers in the model throughout day and night, which are calculated based on Eq. (1). This can be used to interpret the model and the measurements, for example, the contribution of nighttime vegetation respiration to the changes in total column concentrations of CO_2. As described in Sect. 4.2.2, a MB of 3.7 ppm in CO_2 has been found over all the available measurement dates (see Fig. 5), which is defined to be the difference between the measured daily mean XCO_2 and the modelled values. To eliminate the bias (modelled background CO_2 that is too high) and focus on the model–measurement differences due to other causes, this MB is subtracted from the modelled XCO_2 in the day-by-day model–measurement comparison for all sites and for each simulation date.

Figure 6 shows the modelled CO_2 column concentrations from all tracers. In general, there is little difference in the column background concentrations among the five sites over these 6 continuous days (black lines) with an MB and its standard deviation of 404.8 ± 0.19 ppm. Variations of the modelled total CO_2 corrected by the MB (solid red lines) are mostly dominated by biogenic activity (dashed blue lines), with only a minor influence predicted from anthropogenic emissions (dashed yellow lines).

After smoothing, the modelled, bias-corrected $XCO^S_{2,sla}$ (green "+") is slightly higher than the corresponding XCO_2 modelled values (solid red lines), with a RMSE of 0.37 ppm and a MB with its standard deviation of 0.34 ± 0.13 ppm for these 7 consecutive days. This is caused by the less steep shape of the vertical profile of the AK under larger SZAs. There is no obvious difference between the modelled values with and without smoothing during the daytime from around

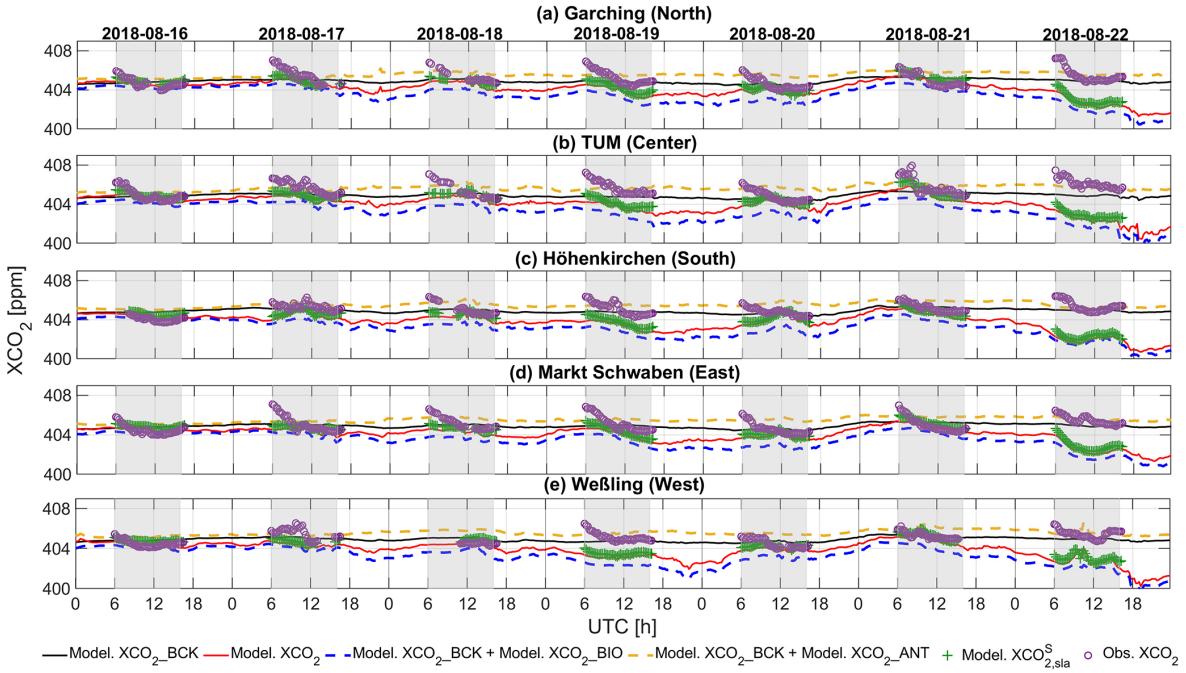

Figure 6. Modelled $XCO^{S}_{2,sla}$, attribution of variations to different tracers, and the measurements at the five MUCCnet sites from 16 to 22 August 2018. The purple circles represent the column measurements from MUCCnet, and the green "+" stands for the modelled $XCO^{S}_{2,sla}$ after subtracting the MB. The other lines in the plot give pressure-weighted modelled column concentrations along the full time series. These are calculated following Eq. (1) (i.e. without smoothing using the SZA-dependent AK) and are corrected by MB. The black curve represents the modelled background (XCO_2_BCK), and the red curve shows the modelled XCO_2. The dashed yellow and blue curves highlight the concentration changes caused by human activities (XCO_2_ANT) and biogenic activities (XCO_2_BIO). The grey shaded areas mark the measurement periods used for comparing observations to model results.

06:00 to 17:00 UTC, which covers most of the period of the day during which measurements can be made.

The modelled $XCO^{S}_{2,sla}$ (green "+") reproduces the variability in the measurements (purple "o") reasonably, with a RMSE of 1.33 ppm, a MB and its SD of -0.79 ± 0.14 ppm, and a coefficient of determination (R^2) of 0.43, as it turns out. However, the measurements often show a steep decrease in concentration during the morning, while the model only shows slight declines. This difference could be the result of an underestimation of the modelled biogenic respiration (RES) from VPRM. During the growing season (June–September), VPRM (Mahadevan et al., 2008) has been found to underestimate RES, especially at night-time, and overestimate GPP during the daytime (Hu et al., 2021). Gourdji et al. (2021) found that the differences of RES at night-time in summertime between the improved and traditional (use in this study) VPRMs can reach more than 3 µmol $(m^2\ s)^{-1}$, depending on vegetation types. This causes an overestimation of the magnitude of NEE (i.e. the difference between RES and GPP), which could explain the difference between the modelled column concentrations and what is observed by MUCCnet. In our case, the observations suggested higher RES fluxes at night-time than what was simulated by the model. This led to much lower modelled column concentrations in the early morning, which was also seen in Hu et al. (2021).

Compared to the modelled values for the other six dates, a slight rise was seen (approximately 1.5 ppm on average) in the morning of 21 August. This was induced by a combined effect of elevated background and biogenic tracer mole fractions. Closer analysis of this case (see the animation of XCO_2_BCK from 19 to 21 August in the Supplement) has shown that the background enhancement entered from the northwest of the outermost boundary in the morning of 19 August and was transported into the innermost domain by the late afternoon of 20 August. This enhanced background signal contributes around two-thirds of the modelled 1.5 ppm rise. The rest is the result of air masses with a strong biospheric CO_2 signature coming from the northwest of our outermost domain. Animations of XCO_2_BIO and XCO_2_BCK from 19 to 21 August are attached in the Supplement to further illustrate this as well.

On 22 August, compared to the simulations for the other days, the modelled $XCO^{S}_{2,sla}$ shows a larger deficit with respect to the measurement in Fig. 6. The model can capture the variation during the day quite well but produces XCO_2 values that are too low when bias corrected through subtraction of the MB. This more extreme mismatch is probably due

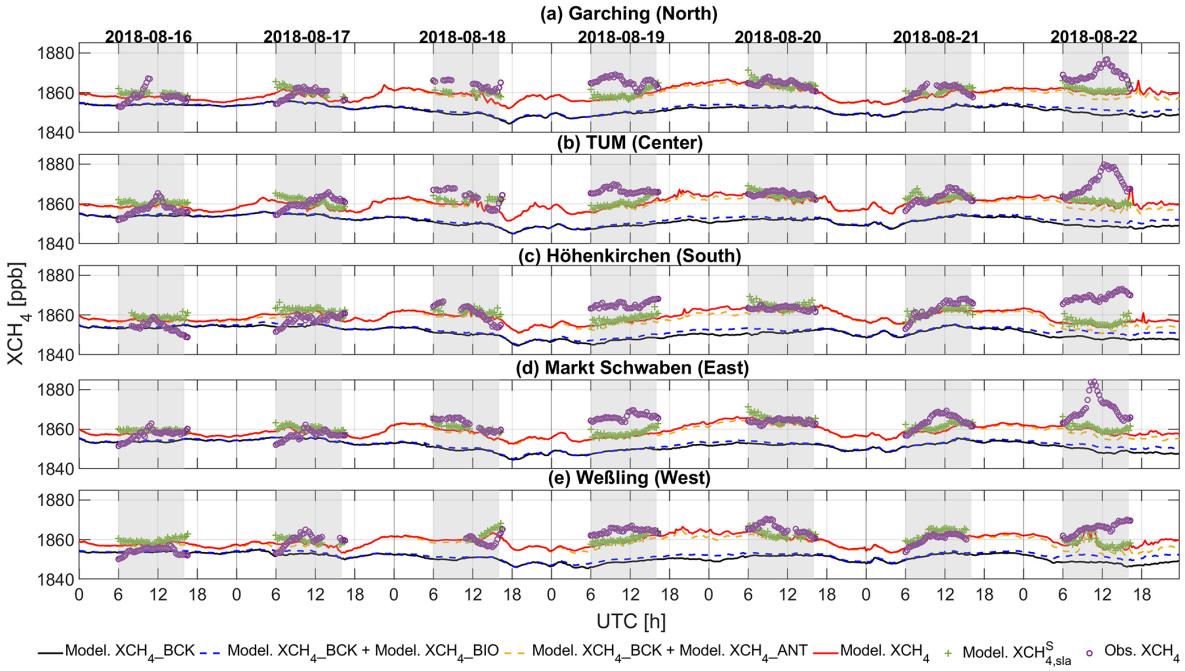

Figure 7. Modelled $XCH^{S}_{4,sla}$, attribution of variations to different tracers and the measurements at five sites of the MUCCnet from 16 to 22 August 2018. The purple "o" represents the column measurements from MUCCnet, and the green "+" stands for the modelled $XCH^{S}_{4,sla}$. The other curves in the plot show the modelled column concentrations calculated following Eq. (1), i.e. without smoothing using the SZA-dependent AK: black curve – modelled background (XCH_4_BCK); red curve – modelled XCH_4. The dashed yellow and blue curves highlight the concentration changes caused by human activities (XCH_4_ANT) and induced by biogenic activities (XCH_4_BIO), including the background. The grey shaded areas mark the measurement periods used for comparing to the simulations.

to the advection of air masses heavily impacted by biogenic activities (and thus with less CO_2) in the model, coming into the domain from, for example, Italy, Slovenia and Croatia. As can be seen in the map of the modelled NEE from VPRM in Fig. S7 of the Supplement, much stronger biogenic fluxes are found in the south of the outermost domain, compared to the other areas. From the view of the model, more CO_2 was taken up, and the affected air masses (i.e. with comparatively less CO_2) are able to reach Munich when the wind is strong enough to drive them past the Alps. In addition, a constant MB over all days, as was applied for the model–measurement comparison, may not always be realistic. An evaluation of the signals within MUCCnet using the DCM is still possible, however, as will be discussed in Sect. 5.

In terms of CH_4, we conduct the same visual analysis (see Fig. 7). The variations of the modelled total XCH_4 (solid red) are dominated by anthropogenic activities (XCH_4_ANT, dashed yellow), and these two variations mostly overlap, since no significant signal induced by wetland emissions (XCH_4_BIO, dashed blue) is predicted by the model. The time series of the modelled $XCH^{S}_{4,sla}$ (green "+") shows general agreement with the measurements (purple "o"). The measurements seem to capture stronger emission signals (e.g. on 22 August), perhaps due to gaps in our knowledge of the spatio-temporal distribution of CH_4 emissions. The modelled values show little diurnal variability at all sites compared to the measurements (RMSE: 6.7 ppb, MB ± SD: -3.3 ± 5.9 ppb, and R^2: 0.31). Regarding the strong enhancements observed by the instruments during the daytime, especially on 22 August, these might be the result of sources which are missing from inventories or are underestimated in their magnitude. In Sect. 5, we attempt to detect such unknown or underestimated emission sources over the domain using DCM.

4.3 Tracer analysis related to human activities

Beyond the major contributors to the concentration enhancements above the background as discussed above, we also analyse the contributions from individual anthropogenic emission processes to understand how these processes impact concentrations quantitatively. To be specific, we use the GNFR emission categories from TNO-GHGco for separately advected tagged tracers. For CO_2, the categories are "A: Power plants", "B: Industry", "C: Other stationary combustion", "D: Road transport", and "E: Other". For CH_4, the emission processes are "A: Power plants", "B: Industry", "C: Agriculture", "D: Waste management", "E: Fugitives and solvents", and "F: Other".

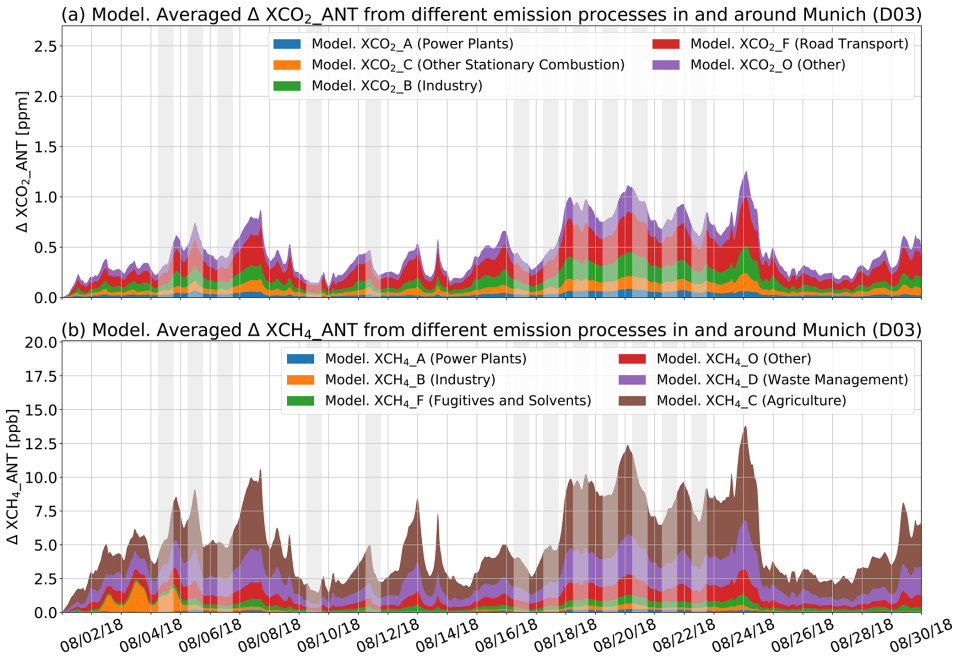

Figure 8. Average modelled concentration contributions by individual anthropogenic emission processes of **(a)** CO_2 (XCO_2_ANT) and **(b)** CH_4 (XCH_4_ANT) from 1 to 30 August 2018 in and around Munich (D03). The grey shaded areas mark the measurement periods used for comparing to the simulations.

The changes in concentrations induced by different human activities along the full time series are plotted in Fig. 8. For CO_2, the emissions from road transport (red) contribute the largest portion (around 37.4 %) of the total concentration enhancements caused by anthropogenic activities in August 2018. This is consistent with the finding that over 30 % of the total GHG emissions are induced by on-road transportation for around one-third of 167 cities worldwide (Wei et al., 2021). This finding may also be due to the seasonal features of emissions in Munich, as there is no heating and less electricity generation in summer. For other contributors, power plants account for around 7 %, other stationary combustion for 13.1 %, and both industry and other contributors for approx. 21 %, respectively. Figure 8b shows that for CH_4 the emissions are dominated by agriculture (brown) and waste management (purple), which are estimated to contribute approx. 50 % and 25 % of the total human-related concentration enhancements.

5 DCM-based evaluation of models, detection, and tracing of additional emission sources

In order to analyse the differences between the measurements and the model, described in Sect. 4.2, we apply DCM. This method allows for a clean interpretation, eliminating biases such as the offset discussed for CO_2 in Sect. 4.2.2. Combining this approach with particle transport modelling using STILT (Fasoli et al., 2018), we explore how we can trace unexpectedly high measured CH_4 signals (see Sect. 4.2.3, Fig. 7) to potential additional sources that are not included in the emission inventory.

In general, DCM is an approach used to assess the emissions over a certain area through the concentration differences (gradients) between down- and upwind GHG measurement sites (Chen et al., 2016; Dietrich et al., 2021). In Zhao et al. (2019), DCM was shown to be a useful post-processing approach in model analysis and model–measurement comparisons, due to its ability to cancel out biases related to initial and boundary conditions. The aim here is to compare our measurements to the model using DCM for selected days from 16 to 22 August 2018, before we attempt to track CH_4 emission sources based on this analysis with the help of STILT.

To begin with, we select up- and downwind sites for our analysis based on the surface wind data presented in Fig. 3 (Sect. 5.1). Furthermore, we select the applicable dates by using the transport model STILT (Sect. 5.2), driven by wind information along the whole column (Sect. 5.2.2). This accounts for wind shear. After comparing the modelled concentration gradients to the observations (Sect. 5.3), we further track the potential location(s) of unknown or underestimated CH_4 sources by using STILT footprint contours. These footprints mark the area of upstream fluxes that influence air masses which arrive at the measurement sites (Sect. 5.4).

5.1 Selection of up- and downwind sites

In DCM, we start by dividing our measurement sites into down- and upwind sites day by day, based on measured wind directions.

As seen in Fig. 5, the measured concentration values at the centre site of MUCCnet (TUM) are found to always be higher than the values observed at the other sites, owing to the dense distribution of emission sources close to the city centre, combined with the higher sensitivity to fluxes in the near-field of the observation location. To better understand the concentration gradients between the down- and upwind sites, we choose to exclude the centre site when calculating the gradients.

The four remaining sites are grouped according to the wind directions observed at LMU. As shown in the wind rose of the measurements (see Fig. 3a.3), the prevailing wind directions during the daytime for our simulation period (WD30) are usually northeasterly or northwesterly. Table 1 shows the list of the down- and upwind sites for different prevailing wind conditions, which are used to calculate the concentration gradients.

Doing this, we assume that the surface winds measured in the city centre are representative of the regional wind conditions over our domain during the day and that they are sufficiently stationary for application of DCM. When rapid, regional-scale horizontal and vertical wind shifts occur, as during a summer cold front passage around the Alps, these assumptions might fail.

Therefore, we set up (Sect. 5.2) and use (Sect. 5.2.2) the STILT model (Fasoli et al., 2018) to assess transport patterns. For our discussion of CO_2 and CH_4 measurements vs. simulations, and most importantly for our attempt to locate unknown or underestimated CH_4 emissions (Sect. 5.4), we have thus been able to select days where the assumptions for DCM are likely to be met. In particular, our method ensures the validity of DCM for the interpretation of the CH_4 concentration peaks.

5.2 Selection of the applicable dates

Before applying DCM to any of the days from 16 to 22 August, we assessed its applicability for each day (see Sect. 5.2.2) by tracking the origin of air masses at different measurement sites with the transport model STILT (see Fasoli et al., 2018) and by assessing the modelled vertical wind profiles used for generating footprints (see Sect. 3.2). Here, we briefly describe the STILT setup.

5.2.1 STILT model setup

In our study, STILT with the R code base (Version 2, as available via https://uataq.github.io/stilt/index.html#/, last access: 11 January 2022; Fasoli, 2018) was implemented using around 168 core hours provided by the high-performance computer centre LRZ. To ensure transport consistency with previously presented results, STILT was driven by the WRF meteorological fields generated for our second domain (D02) at a horizontal resolution of 2 km. An extended discussion of WRF-Chem and STILT is included in Sect. S11 of the Supplement. In order to trace back the origin of air masses at a given spatio-temporal receptor point (corresponding to the time at which an instrument performs a given measurement), STILT uses ensembles of tracer particles which are propagated backwards in time. Specifically, the model provides us with the sensitivity of the analysed slant columns to emissions in lower part of the planetary boundary layer height. These sensitivities are calculated by considering the residence time of released particles when they traverse the lower planetary boundary layer before reaching the measurement location and are further aggregated over the STILT simulation time to produce footprint maps. In our configuration of STILT, we have released 500 particles at 13 altitudes along the slant column, namely at 20, 180, 350, 520, 700, 880, 1060, 1250, 1440, 1620, 1920, 2020, and 2220 m above the ground level for each simulation.

STILT then yields so-called footprint contours (i.e. contours enclosing a certain percentage, for example, 90 %, of the accumulated surface sensitivity) for each altitude layer. Details of the percentile footprint contours are described in Sect. S12 of the Supplement. In order to yield an estimated effective footprint independent of emission height (depending on source and local conditions), we have aggregated these altitude-dependent footprint data for the different layers using the pressure differences between layers as weights (Jones et al., 2021).

5.2.2 Date selection with footprints from STILT

Leveraging the footprint contours from STILT, the differences in the origin and path of air masses arriving at up- and downwind sites can be determined. Understanding these differences is a key prerequisite for determining the location of potential unknown or underestimated GHG sources based on noteworthy signals in the downwind-upwind concentration gradients. Whenever air masses reaching up- and downwind sites have very different areas of influence, the upwind site cannot be used as a relative background site when calculating concentration gradients. In addition, in cases where there are emitters located upstream of an upwind site, the presence of the strong local signal prevents it from being used as a background site. When the footprints fully overlap, however, such that air passes over the upwind to the downwind site, and additional GHG contributions are from in between, DCM can be used. But even when this condition is not strictly met, if differences in the footprint areas are small, the small non-overlapping parts are potential locations for unknown or underestimated GHG emitters and sinks to be pinned down, rendering DCM effective. Signals coming from the overlapping area of the footprints, in contrast, will be visible at multiple measurement sites with a charac-

Table 1. Table of up- and downwind sites depending on wind directions.

Wind direction	Upwind sites	Downwind sites
Northeasterly/easterly (NE/N)	Markt Schwaben (east) Garching (north)	Weßling (west)
Northwesterly/westerly (NW/W)	Weßling (West)	Garching (north) Markt Schwaben (east) Höhenkirchen (south)

teristic time delay. Clearly, for all this to hold, we need to check whether our footprints are realistic. The main prerequisite for this is the accuracy of the WRF wind fields, driving STILT, at different heights. We check this criterion at the end of this section using radiosonde data (see Sect. 3.2).

The approach outlined above can be applied to understand up-/downwind differences and obtain information about GHG sources and transport in the target area. Here, we adopt the following strategy: for each measurement site, we compute the footprint contours with the receptor time in STILT set to the time of the daily XCH_4 peak value [1]. Then, we accept only days for our study where the overlap of these footprints is large. The peak times of the stations are usually different by only a few hours.

Our strategy results in three outcomes: (i) days with unstable wind conditions in time or with large variations of wind directions from one site to another are excluded; (ii) the large overlap and small differences in footprint contours allow for a clear localization of potential origins of differences, as discussed above; and (iii) we can understand whether the peak is of the same origin at all sites. We chose to analyse CH_4 signals at the end of this study (Sect. 5.4), as this offers a realistic possibility of tracking human emission sources (see Sect. 4.2.3) in this exploratory work. In contrast, the current state of the art makes it more difficult to trace anthropogenic effects in CO_2 signals, where biogenic activity plays a much larger role.

We applied our strategy to all measurement days and finally selected 16, 20, and 21 August 2018 as days suitable for further analysis (Sect. 5.3 and 5.4). Figure 9 and the Supplement (in particular Fig. S13 and Sect. S12) lay out the reasons for our decision and show all the footprint contours. In the following paragraphs, we discuss the examples from Fig. 9 (16 and 22 August) further as typical days deemed appropriate (16 August) or inappropriate (22 August) for further analysis using DCM. Besides the footprints, Fig. 9 also shows the peak times used as receptor times for STILT.

On 16 August, with easterly wind prevailing, the instruments deployed upwind (Garching and Markt Schwaben) captured peak CH_4 signals in the first half of the day and a similar signal was then seen at TUM about an hour later (red dots in Fig. 9a). However, the sensor at the downwind site (Weßling) did not detect a major peak. Using the knowledge of station locations and the observed peak times, we would have predicted a peak at Weßling (Fig. 9a, black dot) as follows: the upwind and central sites captured the peaks at around 11:00 and 12:00 UTC, respectively. These air masses would then possibly have reached the downwind site after approximately 2 h (estimated from wind speeds as given in the Supplement, Table S4), corresponding to the distance between TUM and Weßling, i.e. at 14:00 UTC (Fig. 9a, black dot). Note that the receptor times for all up- and downwind sites and dates, determined from observed peaks or estimates in this manner, are listed in Table S7.

On 22 August, the origins of air masses at most of our sites differ significantly (Fig. 9b). The footprints (with receptor times corresponding to the red dots in Fig. 9b, top panel) do not overlap as cleanly, and any "tracing experiment" would be poorly controlled. The peaks seen at the Markt Schwaben (east), TUM (centre), and Garching (north) sites may well be of different origin, given the different footprint shapes. Thus, we do not study this day in further detail.

5.3 Model–measurement comparison of concentration gradients

After checking the prerequisites in the previous sections, we focus our analysis of the differential concentrations (gradients) for the selected dates of 16, 20 and 21 August.

Figure 10 shows $\Delta XCO^{S}_{2,sla}$ for the days selected based on the prevailing wind directions. The modelled concentration gradients of $XCO^{S}_{2,sla}$ between the down- and the upwind sites (solid blue lines in Fig. 10) are driven by both biogenic activities (light green) and human activities (grey). The biogenic part can be attributed to the special spatial distribution of biogenic sinks in Munich and its surroundings (see also Fig. S6 of the Supplement): the southeastern and southwestern parts around Munich are more biologically active and have greater carbon sinks, compared to the other areas. This is an interesting difference to Berlin, where our previous study (Zhao et al., 2019) showed no such signal, corresponding to a relatively even distribution of biogenic fluxes over Berlin. In the model–measurement com-

[1] In a few cases where the peak times have been hardly detectable, they have been inferred using the peak times at nearby sites and considering time delays derived from the daily surface wind speeds from LMU.

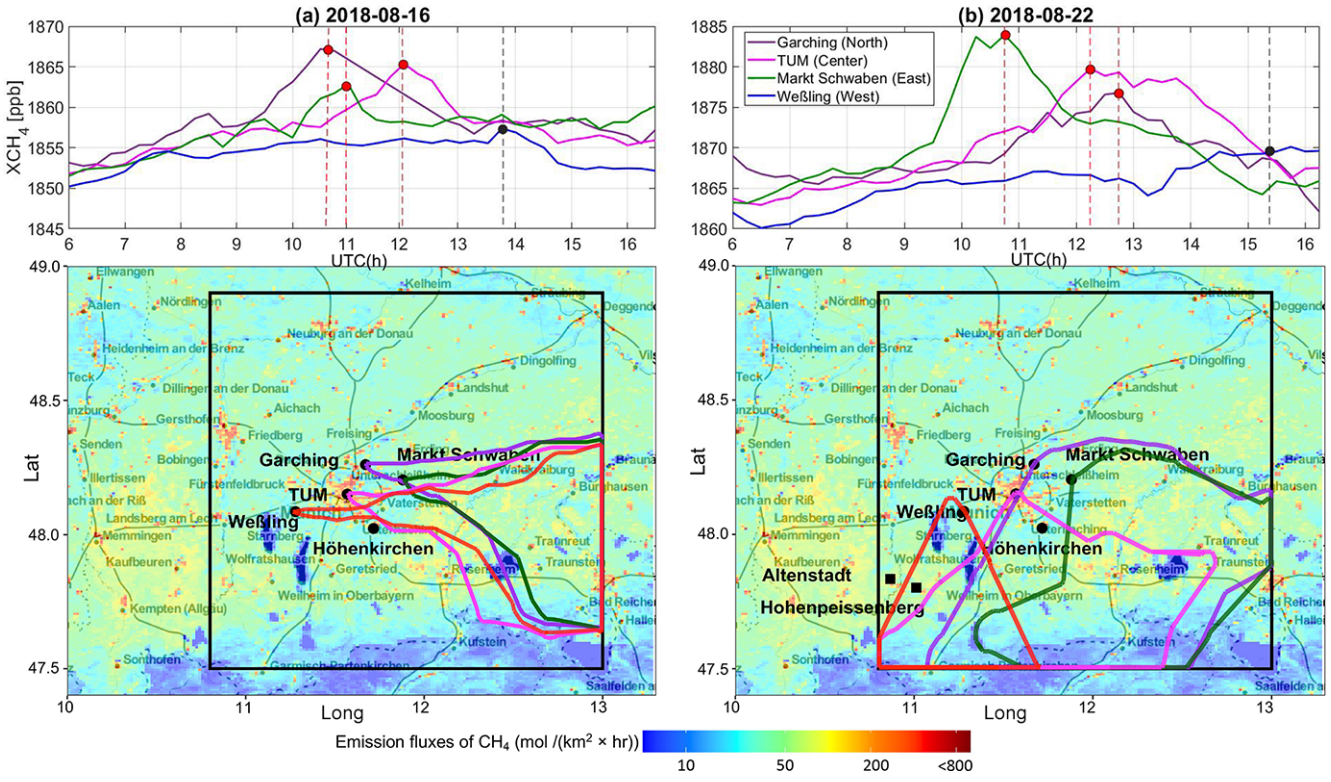

Figure 9. Observed XCH_4 over time (upper panel) and the 90th percentile contours of column footprints (lower panel) on **(a)** 16 August and **(b)** 22 August at up- and downwind sites with different colours: red for Weßling (west), green for Markt Schwaben (east), purple for Garching (north), and pink for TUM (centre). The peaks in the observations are marked by dots (red: clear peaks, black: inferred peaks; see main content/footnote). Two black squares in **(b)** mark the measurement sites of IGRA (see Sect. 3.2). The background maps use tiles from Stamen Design (https://maps.stamen.com/, last access: 8 October 2023, under CC BY 3.0, with data by OpenStreetMap, under ODbL, from 21 December 2021. © OpenStreetMap contributors 2021. Distributed under the Open Data Commons Open Database License (ODbL) v1.0.). The map colouring reflects the emissions from the initial inventory (i.e. TNO-MACCco). The STILT model domains are marked by the thick black boxes.

parison of $\Delta XCO^{S}_{2,sla}$, the model (blue) was able to reproduce the general variations when comparing to the measurements (red) shown in Fig. 10, with a Pearson correlation coefficient (r) of 0.74 and RMSE of 0.37 ppm. However, the modelled and measured concentration gradients show some differences; for example, the modelled concentration gradients between Höhenkirchen and Weßling before 10:00 UTC on 22 August were underestimated compared to the observations. The differences between the modelling results and the measurements could be potentially caused by underestimated concentration gradients from biogenic fluxes in and around the city (light green) in the model. In particular, underestimating RES during night-time (details in Sect. 4.2.3) could result in the underestimation of concentration gradients of CO_2 in the early morning.

As seen in the scatter plot of $\Delta XCH^{S}_{4,sla}$ in Fig. 11a, the modelled values are mostly positive during the day, while the measured concentration gradients between the down- and the upwind sites are mainly negative. The times series of modelled and measured $\Delta XCH^{S}_{4,sla}$ are shown in Fig. S14 (see Sect. S13 of the Supplement). That is, the instruments always measure strong signals at the upwind sites compared to the downwind sites, which cannot be reproduced by the model. As a large methane sink over the city is not expected, the most likely cause for this phenomenon is that emission sources located upstream of an upwind site (i.e. somewhere to the northeast or east of the Garching and Markt Schwaben stations in the case with NE/E winds) are missing or underestimated in the initial emission inventory. Likewise, with W/NW winds, the negative measured concentration gradients between the three down- and one upwind sites are found with −1.89 ppb in daily means and the model fails to reproduce these signals. Again, the measured column concentrations at the upwind sites (i.e. Weßling) are generally higher than at the downwind sites. Especially in the morning of 20 August, a clear strong increase was captured at the upwind side (see Fig. 7). However, none of these features could be replicated by the model. We postulate the presence of an unknown or underestimated source of emissions located upstream of Weßling as the most likely explanation.

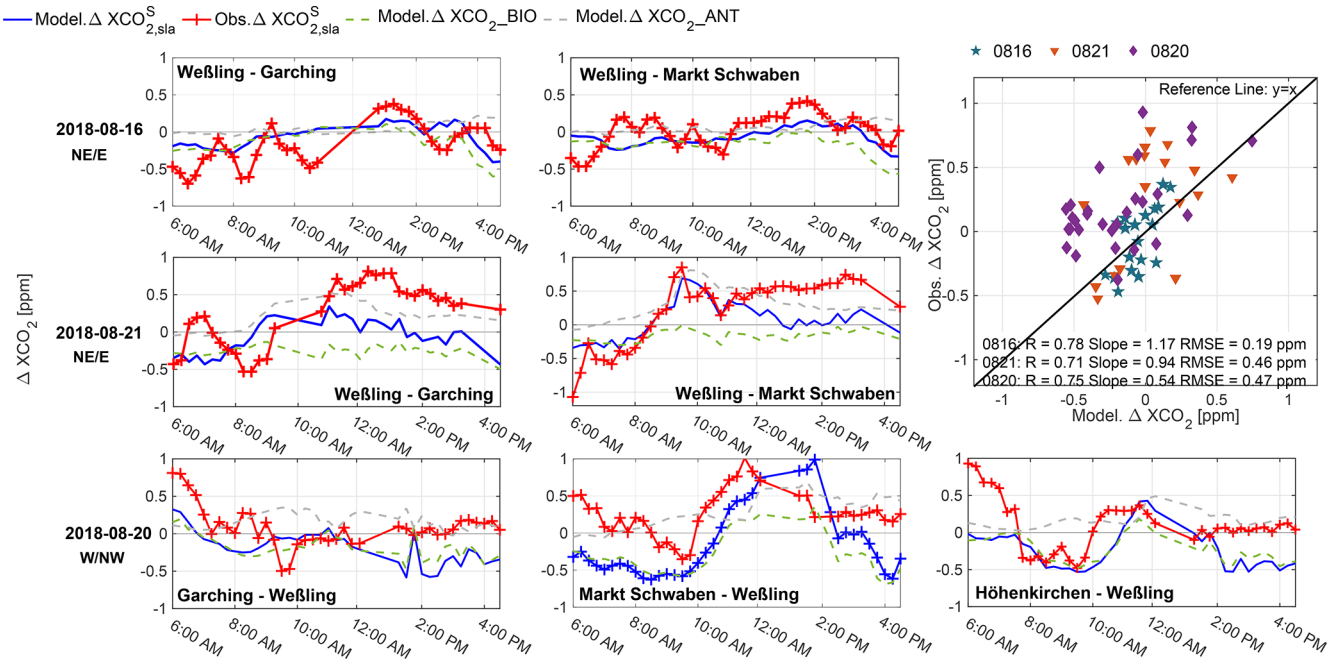

Figure 10. Time series of $\Delta XCO^{S}_{2,sla}$ for three targeted days and their scatter plot: 16 and 21 August with NE/E winds in the upper two rows and 20 August with W/NW winds in the bottom row. The column concentration differences between the down- and the upwind sites are plotted as red solid lines for measurements, solid blue lines for the modelled full signal values, dashed light-green lines for the simulated biogenic signal values, and grey for the modelled contributions related to anthropogenic activities.

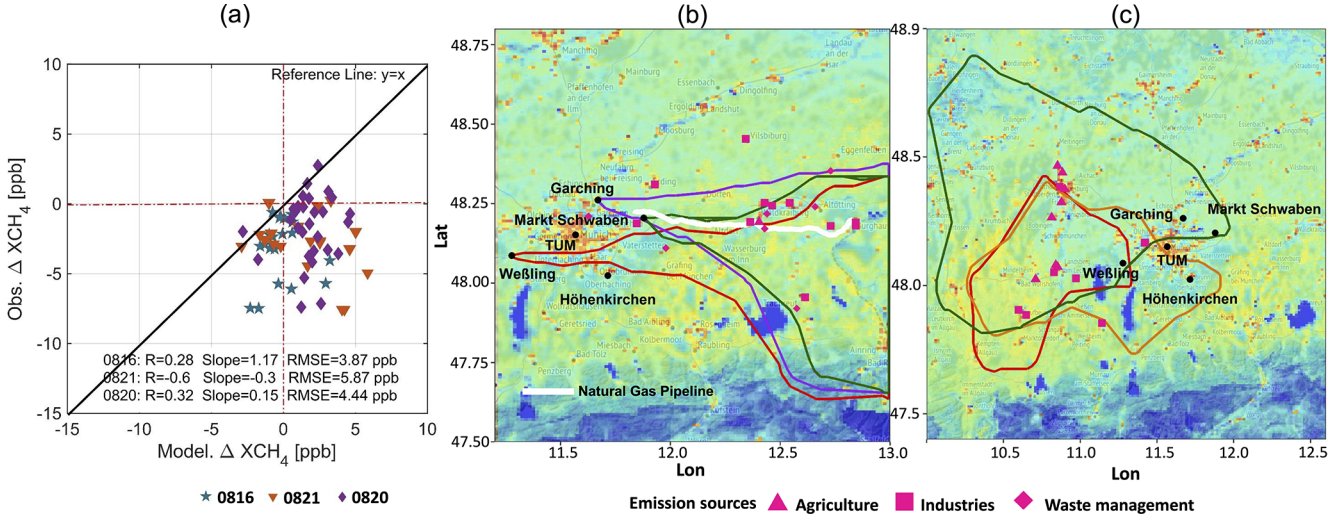

Figure 11. **(a)** Scatter plot of modelled and measured $\Delta XCH^{S}_{4,sla}$ for 3 targeted days and distribution of known emission sources located in the **(b)** eastern and **(c)** western area of Munich and the footprint contours for down- and upwind sites on **(b)** 16 August and **(c)** 20 August: green for Markt Schwaben (east), red for Weßling (west), purple for Garching (north), and yellow for Höhenkirchen (south). The solid white line in **(b)** shows the location of the Burghausen–Finsing–Amerdingen high-pressure natural gas pipeline. The background maps use tiles from Stamen Design (https://maps.stamen.com/, under CC BY 3.0, with data by OpenStreetMap, under ODbL, from 21 December 2021. © OpenStreetMap contributors 2021. Distributed under the Open Data Commons Open Database License (ODbL) v1.0.). The map colouring reflects the emissions from the initial inventory (i.e. TNO-MACCco), with the same colour bar as in Fig. 9.

In addition to the errors caused by the uncertainties in the initial emission inventory, other potential causes could contribute to errors in the concentration and, thus, the gradients as well. The bias brought by the modelled meteorological fields can contribute to the error of the modelled column concentrations and further to discrepancies in the gradients (Wu et al., 2018). Further, our current DCM approach does not take the transport time into account. Moreover, factors such as the mixed layer height and topography could also introduce biases (Hedelius et al., 2017).

5.4 Localizing unknown/underestimated emission sources

To further localize the underestimated or unknown emissions at the upstream areas of both upwind sides (i.e. the western area of Weßling and the eastern area of Markt Schwaben), the footprint contours are used to interpret the transport of air masses. Figure 11 shows the footprint contours of the up- and the downwind sites with two different wind conditions (a) for 16 August and (b) 20 August, and their receptor times are listed in Table S7 of the Supplement.

In this study, the modelled contributions from human activities are initialized with the emission fluxes from the emission inventory TNO_GHGco_v1.1 for the year 2015. The multinational spatially, temporally explicit emission inventory holds large uncertainties, due to the large variability in spatiotemporal distributions of CH_4 emissions from different sectors in different regions that have not yet been fully captured by the emission inventory (Bergamaschi et al., 2022), the disaggregation from annual emissions to hourly values by using temporal profiles, and the temporal inconsistency of emission information from 2015 or even earlier than the study period in 2018. This could result in missing or underestimated emissions, as suggested by the measurements.

After delineating the areas where the uncertain sources could be located, they were further pinpointed based on the updated database and local knowledge. As mentioned in Sect. 4.3, the major contributors of CH_4 related to human activities are waste management, agriculture, and industries (USEPA, 2019). A number of sources from these sectors in and around the areas covered by the footprint contours are identified based on the European industrial emissions portal (available as https://industry.eea.europa.eu/, last access: 14 December 2021), the initial emission inventory, and local knowledge, which are marked in Fig. 11b and c. The waste management here refers to landfill and wastewater treatment facilities, the emissions induced by agriculture come from livestock, and the industry emissions are from heat and gas production and manufacturing, etc. Another potential source of the observed signals that was not represented in our emission inventory was a high-pressure natural gas pipeline that passes through the eastern section of our domain. This pipeline was reportedly under construction and tested in 2018 (constructed by Bayernets GmbH; Macht, 2017; Bayernets, 2018).

Clearly, as a preliminary study, we propose the application of this approach in brief but cannot yet determine the exact cause of the observed peaks that were not reproduced in the model. However, with a longer observation record and refinements to the modelling approach, we see the potential to track down strong emitters of GHGs. It should be noted, however, that accurate estimation of unknown or underestimated sources needs to be performed using a combination of observations and a quantitative footprint analysis. This could provide information for supporting mitigation strategies. Here, the year-round measurements from MUCCnet, which cover a wide range of weather conditions and complete seasonal cycles, will help to complement and improve general inventories.

6 Conclusion

We have developed a WRF modelling framework for Munich to accompany MUCCnet and provide regularly updated concentration maps. Compared to a previous study for the city of Berlin (Zhao et al., 2019), we have introduced additional tagged tracers and improved model inputs. Measurements from MUCCnet and meteorological stations have been used to validate the model. Simulated slant column concentrations, extracted from the model with a smoothing consistent with the instrument characteristics, show encouraging general agreement with observations. We have then focused on comparing modelled column concentrations to measurements and identified the flux categories responsible for the observed signals. The diurnal cycle of CO_2 was not well captured, with the model showing lower concentration enhancements in the morning, while agreeing well in the afternoon. We suspect that this is related to underestimated night-time RES fluxes in VPRM, which has been reported in another recent study.

Our study concludes with a refined application of DCM, aided by air-mass transport tracing with the STILT model. Despite the continuous total-column measurements surrounding the city centre, this analysis highlighted the challenge of extracting the anthropogenic signal from such data. Even though our model was not able to fully reproduce the measured gradients in CH_4 over this complicated source region, this exploratory application enabled us to identify unexpected signals in the measurements and to roughly delineate the potential uncertain source regions in the inventory. The outcomes of this study may provide guidance for other groups considering the optimal instrumentation and analysis frameworks for measuring urban anthropogenic signals.

This study focused on a 1-month period of measurements to refine the modelling approach, but the continuous measurements of MUCCnet are ongoing. This increasingly long and complete data set will enable emission sources to be

monitored on a regular basis. The evaluation of model output and measurements for longer time periods, with various wind conditions, will allow for a better localization of sources and for an improvement of emission inventories. We are looking forward to conducting further studies in this direction, in particular as Munich is one of the three main pilot cities in the EU H2020 project "ICOS Cities". Within this project, more measurement sites will be operated in and around Munich in the coming years. More comprehensive comparisons for meteorological parameters can be expected. A study into the use of the simultaneously measured total column carbon monoxide (XCO) to constrain emissions from combustion processes can be carried out. Inclusion of measurements from aircraft (e.g. In-service Aircraft for a Global Observing System (IAGOS) project – http://www.iagos.org, last access: 11 September 2023) and satellites (e.g. the Orbiting Carbon Observatory-2 and Orbiting Carbon Observatory-3 (OCO-2 and OCO-3) operated by NASA) will help to further validate and make use of our models. Our data–model framework will bring us closer to the aim of effectively tracing GHG emissions and improving emission inventories.

Code and data availability. The model data used to support the results described in this paper are available upon request to the first and corresponding authors. The measured column-averaged dry-air mole fractions of CO_2 and CH_4 recorded during an urban measurement campaign in Munich in August 2018 can be found at https://doi.org/10.1594/PANGAEA.962966 (Dietrich et al., 2023). STILT with the R code base Version 2 (https://doi.org/10.5281/zenodo.1238047, Fasoli, 2018) can be assessed via its official GitHub at https://github.com/uataq/stilt (last access: 4 November 2023).

Supplement. The supplement related to this article is available online at: https://doi.org/10.5194/acp-23-14325-2023-supplement.

Author contributions. The modelling framework designed for Munich is mainly built by XZ with joint effort from JM, MG, CG, SH, and JC. Regarding the initialization, JM, MG, and CG retrieved the CAMS fields and preprocessed the vegetation indices and the necessary variables for the Kaplan model. JC, FD, and AW helped with the interpretation of the measurements. CG, JG, JM, AS, and XZ put effort into the improvement of VPRM. SH gave guidance on running the WRF model on the Linux Cluster of Leibniz Supercomputing Centre. XZ, JC, and SH designed the computational framework. XZ and JC performed the analysis of the results with support of JM, CG, and MG. As project PI, JC supervised the work and acquired the funding. With the input from all authors, XZ wrote the manuscript. All authors provided critical feedback and helped shape the research, analysis, and manuscript.

Competing interests. At least one of the (co-)authors is a member of the editorial board of *Atmospheric Chemistry and Physics*. The peer-review process was guided by an independent editor, and the author also have no other competing interests to declare.

Disclaimer. Publisher's note: Copernicus Publications remains neutral with regard to jurisdictional claims in published maps and institutional affiliations.

Acknowledgements. TUM authors as well as MUCCnet are supported by the German Research Foundation (DFG, grant nos. CH 1792/2-1, INST 95/1544). WRF and STILT workflows were run on the CoolMUC-2 High-Performance Computing (HPC) system, part of the Linux Cluster at LRZ, where two nodes of Environmental Sensing and Modeling are also housed.

Ankit Shekhar acknowledges funding from the ETH Zürich project FEVER ETH-27 19-1.

Financial support. This research has been supported by the German Research Foundation (DFG, grant nos. CH1792/2-1 and INST 95/1544), the ETH Zürich (project FEVER ETH-27 19-1), and the EU Horizon 2020 Programme (ICOS Cities Project under grant 101037319).

This work was supported by the Technical University of Munich (TUM) in the framework of the Open Access Publishing Program.

Review statement. This paper was edited by Manvendra Krishna Dubey and reviewed by two anonymous referees.

References

Alberti, C., Hase, F., Frey, M., Dubravica, D., Blumenstock, T., Dehn, A., Castracane, P., Surawicz, G., Harig, R., Baier, B. C., Bès, C., Bi, J., Boesch, H., Butz, A., Cai, Z., Chen, J., Crowell, S. M., Deutscher, N. M., Ene, D., Franklin, J. E., García, O., Griffith, D., Grouiez, B., Grutter, M., Hamdouni, A., Houweling, S., Humpage, N., Jacobs, N., Jeong, S., Joly, L., Jones, N. B., Jouglet, D., Kivi, R., Kleinschek, R., Lopez, M., Medeiros, D. J., Morino, I., Mostafavipak, N., Müller, A., Ohyama, H., Palmer, P. I., Pathakoti, M., Pollard, D. F., Raffalski, U., Ramonet, M., Ramsay, R., Sha, M. K., Shiomi, K., Simpson, W., Stremme, W., Sun, Y., Tanimoto, H., Té, Y., Tsidu, G. M., Velazco, V. A., Vogel, F., Watanabe, M., Wei, C., Wunch, D., Yamasoe, M., Zhang, L., and Orphal, J.: Improved calibration procedures for the EM27/SUN spectrometers of the COllaborative Carbon Column Observing Network (COCCON), Atmos. Meas. Tech., 15, 2433–2463, https://doi.org/10.5194/amt-15-2433-2022, 2022.

Bayernets: Erdgasfernleitung Monaco Von Burghausen Nach Finsing, bayernets GmbH, https://www.bayernets.de/artikel?tx_news_pi1%5Baction%5D=detail&tx_news_pi1%5Bcontroller%5D=News&tx_news_pi1%5Bnews%5D=7&cHash=dbd930d473607825cf1354f7db2ab58e (last access: 11 September 2023), 2018.

Beck, V., Koch, T., Kretschmer, R., Marshall, J.and Ahmadov, R., Gerbig, C., Pillai, D., and Heimann, M.: The WRF Greenhouse Gas Model (WRF-GHG). Technical Report No. 25, Tech. rep., Max Planck Institute for Biogeochemistry, Jena, Germany, https://www.bgc-jena.mpg.de/bgc-systems/pmwiki2/uploads/Download/Wrf-ghg/WRF-GHG_Techn_Report.pdf (last access: 11 September 2023), 2012.

Beck, V., Gerbig, C., Koch, T., Bela, M. M., Longo, K. M., Freitas, S. R., Kaplan, J. O., Prigent, C., Bergamaschi, P., and Heimann, M.: WRF-Chem simulations in the Amazon region during wet and dry season transitions: evaluation of methane models and wetland inundation maps, Atmos. Chem. Phys., 13, 7961–7982, https://doi.org/10.5194/acp-13-7961-2013, 2013.

Bergamaschi, P., Segers, A., Brunner, D., Haussaire, J.-M., Henne, S., Ramonet, M., Arnold, T., Biermann, T., Chen, H., Conil, S., Delmotte, M., Forster, G., Frumau, A., Kubistin, D., Lan, X., Leuenberger, M., Lindauer, M., Lopez, M., Manca, G., Müller-Williams, J., O'Doherty, S., Scheeren, B., Steinbacher, M., Trisolino, P., Vítková, G., and Yver Kwok, C.: High-resolution inverse modelling of European CH_4 emissions using the novel FLEXPART-COSMO TM5 4DVAR inverse modelling system, Atmos. Chem. Phys., 22, 13243–13268, https://doi.org/10.5194/acp-22-13243-2022, 2022.

Borsdorff, T., Hasekamp, O. P., Wassmann, A., and Landgraf, J.: Insights into Tikhonov regularization: application to trace gas column retrieval and the efficient calculation of total column averaging kernels, Atmos. Meas. Tech., 7, 523–535, https://doi.org/10.5194/amt-7-523-2014, 2014.

Brousse, O., Martilli, A., Foley, M., Mills, G., and Bechtel, B.: WUDAPT, an efficient land use producing data tool for mesoscale models? Integration of urban LCZ in WRF over Madrid, Urban Climate, 17, 116–134, https://doi.org/10.1016/j.uclim.2016.04.001, 2016.

Browne, P. A., de Rosnay, P., Zuo, H., Bennett, A., and Dawson, A.: Weakly coupled ocean–atmosphere data assimilation in the ECMWF NWP system, Remote Sens.-Basel, 11, 234, https://doi.org/10.3390/rs11030234, 2019.

Brunner, D., Kuhlmann, G., Marshall, J., Clément, V., Fuhrer, O., Broquet, G., Löscher, A., and Meijer, Y.: Accounting for the vertical distribution of emissions in atmospheric CO_2 simulations, Atmos. Chem. Phys., 19, 4541–4559, https://doi.org/10.5194/acp-19-4541-2019, 2019.

Chen, J., Viatte, C., Hedelius, J. K., Jones, T., Franklin, J. E., Parker, H., Gottlieb, E. W., Wennberg, P. O., Dubey, M. K., and Wofsy, S. C.: Differential column measurements using compact solar-tracking spectrometers, Atmos. Chem. Phys., 16, 8479–8498, https://doi.org/10.5194/acp-16-8479-2016, 2016.

Chen, J., Gerbig, C., Marshall, J., and Totsche, K. U.: Short-term forecasting of regional biospheric CO_2 fluxes in Europe using a light-use-efficiency model (VPRM, MPI-BGC version 1.2), Geosci. Model Dev., 13, 4091–4106, https://doi.org/10.5194/gmd-13-4091-2020, 2020.

Ching, J., Mills, G., Bechtel, B., See, L., Feddema, J., Wang, X., Ren, C., Brousse, O., Martilli, A., and Neophytou, M.: WUDAPT: An urban weather, climate, and environmental modeling infrastructure for the anthropocene, B. A. Meteorol. Soc., 99, 1907–1924, https://doi.org/10.1175/BAMS-D-16-0236.1, 2018.

DeCola, P., Tarasova, O., Brunner, D., Maksyutov, S., Manning, A., Vogel, F., Gurney, K., Turnbull, J., Zavala-Araiza, D., Kort, E., Robinson, R., Canadell, P., Ciais, P., Vladu, F., Houweling, S., Lauvaux, T., and Mueller, K.: An Integrated Global Greenhouse Gas Information System (IG3IS) Science Implementation Plan Approved by EC-70, World Meteorological Organization (WMO), https://library.wmo.int/viewer/56863?medianame=gaw_245_en_#page=1&viewer=picture&o=&n=0&q= (last access: 4 November 2023), 2018.

de Coninck, H., Revi, A., Babiker, M., Bertoldi, P., Buckeridge, M., Cartwright, A., Dong, W., Ford, J., Fuss, S., Hourcade, J.-C., Ley, D., Mechler, R., Newman, P., Revokatova, A., Schultz, S., Steg, L., and Sugiyama, T.: Strengthening and Implementing the Global Response, in: Global Warming of 1.5 °C. An IPCC Special Report on the impacts of global warming of 1.5 °C above pre-industrial levels and related global greenhouse gas emission pathways, in the context of strengthening the global response to the threat of climate change, sustainable development, and efforts to eradicate poverty, edited by: Masson-Delmotte, V., Zhai, P., Pörtner, H.-O., Roberts, D., Skea, J., Shukla, P. R., Pirani, A., Moufouma-Okia, W., Péan, C., Pidcock, R., Connors, S., Matthews, J. B. R., Chen, Y., Zhou, X., Gomis, M. I., Lonnoy, E., Maycock, T., Tignor, M., and Waterfield, T., Cambridge University Press, Cambridge, UK and New York, NY, USA, 313–444, https://doi.org/10.1017/9781009157940.006, 2018.

Dekker, I. N., Houweling, S., Aben, I., Röckmann, T., Krol, M., Martínez-Alonso, S., Deeter, M. N., and Worden, H. M.: Quantification of CO emissions from the city of Madrid using MOPITT satellite retrievals and WRF simulations, Atmos. Chem. Phys., 17, 14675–14694, https://doi.org/10.5194/acp-17-14675-2017, 2017.

Demuzere, M., Bechtel, B., Middel, A., and Mills, G.: Mapping Europe into local climate zones, PLOS ONE, 14, e0214474, https://doi.org/10.1371/journal.pone.0214474, 2019.

Dietrich, F., Chen, J., Reger, B., Matzke, J., Forstmaier, A., Bi, X., Luther, A., Frey, M., Hase, F., and Butz, A.: First fully-automated differential column network for measuring GHG emissions tested in Munich, in: Geophysical Research Abstracts, European Geosciences Union – General Assembly 2019, vol. 21, https://doi.org/10.13140/RG.2.2.26867.17441, 2019.

Dietrich, F., Chen, J., Voggenreiter, B., Aigner, P., Nachtigall, N., and Reger, B.: MUCCnet: Munich Urban Carbon Column network, Atmos. Meas. Tech., 14, 1111–1126, https://doi.org/10.5194/amt-14-1111-2021, 2021.

Dietrich, F., Chen, J., Forstmaier, A., Bi, X., Reger, B., Luther, A., Matzke, J., Ramezani, M., Hase, F., and Butz, A.: Column-averaged dry-air mole fractions of CO_2, CH_4 and CO recorded during an urban measurement campaign in Munich in August 2018 with five solar-tracking Fourier transform spectrometers (EM27/SUN), PANGAEA [data set], https://doi.org/10.1594/PANGAEA.962966, 2023.

Durre, I., Yin, X., Vose, R. S., Applequist, S., and Arnfield, J.: Enhancing the data coverage in the Integrated Global Radiosonde Archive, J. Atmos. Ocean. Tech., 35, 1753–1770, https://doi.org/10.1175/JTECH-D-17-0223.1, 2018.

EU Commission: A Clean Planet for all-A European strategic long-term vision for a prosperous, modern, competitive and climate neutral economy, Tech. rep., Technical Report, European Commission, Brussels. Federal Ministry of Interior Building and Community (IBC)-Sustainable Building Assessment System (BNB), https://eur-lex.europa.eu/legal-content/EN/

TXT/?uri=CELEX%3A52018DC0773 (last access: 4 November 2023), 2018.

Fasoli, B.: uataq/stilt: Geoscientific Model Development 2018 (v1.1), Zenodo [code], https://doi.org/10.5281/zenodo.1238047, 2018.

Fasoli, B., Lin, J. C., Bowling, D. R., Mitchell, L., and Mendoza, D.: Simulating atmospheric tracer concentrations for spatially distributed receptors: updates to the Stochastic Time-Inverted Lagrangian Transport model's R interface (STILT-R version 2), Geosci. Model Dev., 11, 2813–2824, https://doi.org/10.5194/gmd-11-2813-2018, 2018.

Frey, M., Hase, F., Blumenstock, T., Groß, J., Kiel, M., Mengistu Tsidu, G., Schäfer, K., Sha, M. K., and Orphal, J.: Calibration and instrumental line shape characterization of a set of portable FTIR spectrometers for detecting greenhouse gas emissions, Atmos. Meas. Tech., 8, 3047–3057, https://doi.org/10.5194/amt-8-3047-2015, 2015.

Frey, M., Sha, M. K., Hase, F., Kiel, M., Blumenstock, T., Harig, R., Surawicz, G., Deutscher, N. M., Shiomi, K., Franklin, J. E., Bösch, H., Chen, J., Grutter, M., Ohyama, H., Sun, Y., Butz, A., Mengistu Tsidu, G., Ene, D., Wunch, D., Cao, Z., Garcia, O., Ramonet, M., Vogel, F., and Orphal, J.: Building the COllaborative Carbon Column Observing Network (COCCON): long-term stability and ensemble performance of the EM27/SUN Fourier transform spectrometer, Atmos. Meas. Tech., 12, 1513–1530, https://doi.org/10.5194/amt-12-1513-2019, 2019.

Gałkowski, M., Jordan, A., Rothe, M., Marshall, J., Koch, F.-T., Chen, J., Agusti-Panareda, A., Fix, A., and Gerbig, C.: In situ observations of greenhouse gases over Europe during the CoMet 1.0 campaign aboard the HALO aircraft, Atmos. Meas. Tech., 14, 1525–1544, https://doi.org/10.5194/amt-14-1525-2021, 2021.

Georgiou, G. K., Christoudias, T., Proestos, Y., Kushta, J., Hadjinicolaou, P., and Lelieveld, J.: Air quality modelling in the summer over the eastern Mediterranean using WRF-Chem: chemistry and aerosol mechanism intercomparison, Atmos. Chem. Phys., 18, 1555–1571, https://doi.org/10.5194/acp-18-1555-2018, 2018.

Gisi, M., Hase, F., Dohe, S., Blumenstock, T., Simon, A., and Keens, A.: XCO_2-measurements with a tabletop FTS using solar absorption spectroscopy, Atmos. Meas. Tech., 5, 2969–2980, https://doi.org/10.5194/amt-5-2969-2012, 2012.

Gourdji, S., Karion, A., Lopez-Coto, I., Ghosh, S., Mueller, K. L., Zhou, Y., Williams, C. A., Baker, I. T., Haynes, K., and Whetstone, J.: A modified Vegetation Photosynthesis and Respiration Model (VPRM) for the eastern USA and Canada, evaluated with comparison to atmospheric observations and other biospheric models, Earth and Space Science Open Archive, p. 50, https://doi.org/10.1002/essoar.10506768.1, 2021.

Hase, F., Hannigan, J., Coffey, M., Goldman, A., Höpfner, M., Jones, N., Rinsland, C., and Wood, S.: Intercomparison of retrieval codes used for the analysis of high-resolution, ground-based FTIR measurements, J. Quant. Spectrosc. Ra., 87, 25–52, https://doi.org/10.1016/j.jqsrt.2003.12.008, 2004.

Hase, F., Frey, M., Blumenstock, T., Groß, J., Kiel, M., Kohlhepp, R., Mengistu Tsidu, G., Schäfer, K., Sha, M. K., and Orphal, J.: Application of portable FTIR spectrometers for detecting greenhouse gas emissions of the major city Berlin, Atmos. Meas. Tech., 8, 3059–3068, https://doi.org/10.5194/amt-8-3059-2015, 2015.

Hase, F., Frey, M., Kiel, M., Blumenstock, T., Harig, R., Keens, A., and Orphal, J.: Addition of a channel for XCO observations to a portable FTIR spectrometer for greenhouse gas measurements, Atmos. Meas. Tech., 9, 2303–2313, https://doi.org/10.5194/amt-9-2303-2016, 2016.

Hedelius, J. K., Viatte, C., Wunch, D., Roehl, C. M., Toon, G. C., Chen, J., Jones, T., Wofsy, S. C., Franklin, J. E., Parker, H., Dubey, M. K., and Wennberg, P. O.: Assessment of errors and biases in retrievals of X_{CO_2}, X_{CH_4}, X_{CO}, and X_{N_2O} from a $0.5\,cm^{-1}$ resolution solar-viewing spectrometer, Atmos. Meas. Tech., 9, 3527–3546, https://doi.org/10.5194/amt-9-3527-2016, 2016.

Hedelius, J. K., Feng, S., Roehl, C. M., Wunch, D., Hillyard, P. W., Podolske, J. R., Iraci, L. T., Patarasuk, R., Rao, P., O'Keeffe, D., Gurney, K. R., Lauvaux, T., and Wennberg, P. O.: Emissions and topographic effects on column CO_2 variations, with a focus on the Southern California Megacity, J. Geophys. Res.-Atmos., 122, 7200–7215, https://doi.org/10.1002/2017jd026455, 2017.

Heerah, S., Frausto-Vicencio, I., Jeong, S., Marklein, A. R., Ding, Y., Meyer, A. G., Parker, H. A., Fischer, M. L., Franklin, J. E., Hopkins, F. M., and Dubey, M.: Dairy methane emissions in California's San Joaquin Valley inferred with ground-based remote sensing observations in the summer and winter, J. Geophys. Res.-Atmos., 126, e2021JD034785, https://doi.org/10.1029/2021JD034785, 2021.

Heimburger, A. M., Harvey, R. M., Shepson, P. B., Stirm, B. H., Gore, C., Turnbull, J., Cambaliza, M. O., Salmon, O. E., Kerlo, A.-E. M., Lavoie, T. N., Davis, K. J., Lauvaux, T., Karion, A., Sweeney, C., Brewer, W. A., Hardesty, R. M., and Gurney, K. R.: Assessing the optimized precision of the aircraft mass balance method for measurement of urban greenhouse gas emission rates through averaging, Elem. Sci. Anth., 5, 26, https://doi.org/10.1525/elementa.134, 2017.

Heinle, L. and Chen, J.: Automated enclosure and protection system for compact solar-tracking spectrometers, Atmos. Meas. Tech., 11, 2173–2185, https://doi.org/10.5194/amt-11-2173-2018, 2018.

Hersbach, H., Bell, B., Berrisford, P., Hirahara, S., Horányi, A., Muñoz-Sabater, J., Nicolas, J., Peubey, C., Radu, R., and Schepers, D.: The ERA5 global reanalysis, Q. J. Roy. Meteor. Soc., 146, 1999–2049, https://doi.org/10.1002/qj.3803, 2020.

Hu, X.-M., Nielsen-Gammon, J. W., and Zhang, F.: Evaluation of Three Planetary Boundary Layer Schemes in the WRF Model, J. Appl. Meteorol. Clim., 49, 1831–1844, https://doi.org/10.1175/2010JAMC2432.1, 2010.

Hu, X.-M., Gourdji, S. M., Davis, K. J., Wang, Q., Zhang, Y., Xue, M., Feng, S., Moore, B., and Crowell, S. M.: Implementation of improved parameterization of terrestrial flux in WRF-VPRM improves the simulation of nighttime CO_2 peaks and a daytime CO_2 band ahead of a cold front, J. Geophys. Res.-Atmos., 126, e2020JD034362, https://doi.org/10.1029/2020JD034362, 2021.

IRENA: Renewable energy in cities, International Renewable Agency: Abu Dhabi, UAE, https://www.irena.org/publications/2016/Jul/Renewable-Energy-Statistics-2016 (last access: 10 September 2023), 2016.

Janssens-Maenhout, G., Crippa, M., Guizzardi, D., Muntean, M., Schaaf, E., Dentener, F., Bergamaschi, P., Pagliari, V., Olivier, J. G. J., Peters, J. A. H. W., van Aardenne, J. A., Monni, S., Doering, U., Petrescu, A. M. R., Solazzo, E., and Oreggioni, G. D.:

EDGAR v4.3.2 Global Atlas of the three major greenhouse gas emissions for the period 1970–2012, Earth Syst. Sci. Data, 11, 959–1002, https://doi.org/10.5194/essd-11-959-2019, 2019.

Jiménez, P. A. and Dudhia, J.: On the ability of the WRF model to reproduce the surface wind direction over complex terrain, J. Appl. Meteorol. Clim., 52, 1610–1617, https://doi.org/10.1175/JAMC-D-12-0266.1, 2013.

Jones, T. S., Franklin, J. E., Chen, J., Dietrich, F., Hajny, K. D., Paetzold, J. C., Wenzel, A., Gately, C., Gottlieb, E., Parker, H., Dubey, M., Hase, F., Shepson, P. B., Mielke, L. H., and Wofsy, S. C.: Assessing urban methane emissions using column-observing portable Fourier transform infrared (FTIR) spectrometers and a novel Bayesian inversion framework, Atmos. Chem. Phys., 21, 13131–13147, https://doi.org/10.5194/acp-21-13131-2021, 2021.

Jung, M., Henkel, K., Herold, M., and Churkina, G.: Exploiting synergies of global land cover products for carbon cycle modeling, Remote Sens. Environ., 101, 534–553, https://doi.org/10.1016/j.rse.2006.01.020, 2006.

Kaplan, J., Folberth, G., and Hauglustaine, D.: Role of methane and biogenic volatile organic compound sources in late glacial and Holocene fluctuations of atmospheric methane concentrations, Global Biogeochem. Cy., 20, GB2016, https://doi.org/10.1029/2005GB002590, 2006.

Klausner, T., Mertens, M., Huntrieser, H., Galkowski, M., Kuhlmann, G., Baumann, R., Fiehn, A., Jöckel, P., Pühl, M., and Roiger, A.: Urban greenhouse gas emissions from the Berlin area: A case study using airborne CO_2 and CH_4 in situ observations in summer 2018, Elem. Sci. Anth., 8, 15, https://doi.org/10.1525/elementa.411, 2020.

Laughner, J. L., Roche, S., Kiel, M., Toon, G. C., Wunch, D., Baier, B. C., Biraud, S., Chen, H., Kivi, R., Laemmel, T., McKain, K., Quéhé, P.-Y., Rousogenous, C., Stephens, B. B., Walker, K., and Wennberg, P. O.: A new algorithm to generate a priori trace gas profiles for the GGG2020 retrieval algorithm, Atmos. Meas. Tech., 16, 1121–1146, https://doi.org/10.5194/amt-16-1121-2023, 2023.

Lauvaux, T., Miles, N. L., Deng, A., Richardson, S. J., Cambaliza, M. O., Davis, K. J., Gaudet, B., Gurney, K. R., Huang, J., O'Keefe, D., Song, Y., Karion, A., Oda, T., Patarasuk, R., Razlivanov, I., Sarmiento, D., Shepson, P., Sweeney, C., Turnbull, J., and Wu, K.: High-resolution atmospheric inversion of urban CO_2 emissions during the dormant season of the Indianapolis Flux Experiment (INFLUX), J. Geophys. Res.-Atmos., 121, 5213–5236, https://doi.org/10.1002/2015JD024473, 2016.

Macht, V.: Die Pipeline ist im Anmarsch, Merkur.de, https://www.merkur.de/lokales/erding/isen-ort86592/erdgasfernleitung-monaco-pipeline-ist-im-anmarsch-8372127.html, (last access: 11 April 2022), 2017.

Mahadevan, P., Wofsy, S. C., Matross, D. M., Xiao, X., Dunn, A. L., Lin, J. C., Gerbig, C., Munger, J. W., Chow, V. Y., and Gottlieb, E. W.: A satellite-based biosphere parameterization for net ecosystem CO_2 exchange: Vegetation Photosynthesis and Respiration Model (VPRM), GLOBAL Biogeochem. Cy., 22, GB2005, https://doi.org/10.1029/2006GB002735, 2008.

Masson-Delmotte, V., Zhai, P., Pörtner, H.-O., Roberts, D., Skea, J., Shukla, P., Pirani, A., Moufouma-Okia, W., Péan, C., Pidcock, R., Connors, S., Matthews, J., Chen, Y., Zhou, X., Gomis, M., Lonnoy, E., Maycock, T., and Tignor, M.and Waterfield, T.: IPCC, 2018: Summary for policymakers, in: Global warming of 1.5 °C. An IPCC Special Report on the impacts of global warming of 1.5 °C above pre-industrial levels and related global greenhouse gas emission pathways, in the context of strengthening the global response to the threat of climate change, sustainable development, and efforts to eradicate poverty, World Meteorological Organization, Geneva, Switzerland, 3–24, https://doi.org/10.1017/9781009157940.001, 2018.

Masson-Delmotte, V., Zhai, P., Pirani, A., Connors, S. L., Péan, C., Berger, S., Caud, N., Chen, Y., Goldfarb, L., Gomis, M. I., Huang, M., Leitzell, K., Lonnoy, E., Matthews, J., Maycock, T. K., Waterfield, T., Yelekçi, O., Yu, R., and Zhou, B.: Summary for Policymakers, in: Climate Change 2021: The Physical Science Basis. Contribution of Working Group I to the Sixth Assessment Report of the Intergovernmental Panel on Climate Change, Cambridge University Press, 1–24, https://doi.org/10.1017/9781009157896.001, 2021.

Mughal, M. O.: Modelling the Urban Heat Island in Singapore-state of the art WRF model technical details, Technical Report Cooling Singapore, Singapore-ETH Centre (SEC), Cooling Singapore (CS), 500, https://doi.org/10.3929/ethz-b-000412358, 2020.

Ohyama, H., Morino, I., Velazco, V. A., Klausner, T., Bagtasa, G., Kiel, M., Frey, M., Hori, A., Uchino, O., Matsunaga, T., Deutscher, N. M., DiGangi, J. P., Choi, Y., Diskin, G. S., Pusede, S. E., Fiehn, A., Roiger, A., Lichtenstern, M., Schlager, H., Wang, P. K., Chou, C. C.-K., Andrés-Hernández, M. D., and Burrows, J. P.: Validation of XCO_2 and XCH_4 retrieved from a portable Fourier transform spectrometer with those from in situ profiles from aircraft-borne instruments, Atmos. Meas. Tech., 13, 5149–5163, https://doi.org/10.5194/amt-13-5149-2020, 2020.

Peckham, S., Grell, G., McKeen, S., Ahmadov, R., Barth, M., Pfister, G., Wiedinmyer, C., Fast, J., Gustafson, W., Ghan, S., Zaveri, R., Easter, R., Barnard, J., Chapman, E., Hewson, M., Schmitz, R., Salzmann, M., and Freitas, S.: WRF-Chem Version 3.9.1.1 User's Guide, Tech. rep., National Center for Atmospheric Research, https://ruc.noaa.gov/wrf/wrf-chem/Users_guide.pdf (last access: 10 September 2023), 2017.

Rémy, S., Kipling, Z., Flemming, J., Boucher, O., Nabat, P., Michou, M., Bozzo, A., Ades, M., Huijnen, V., Benedetti, A., Engelen, R., Peuch, V.-H., and Morcrette, J.-J.: Description and evaluation of the tropospheric aerosol scheme in the European Centre for Medium-Range Weather Forecasts (ECMWF) Integrated Forecasting System (IFS-AER, cycle 45R1), Geosci. Model Dev., 12, 4627–4659, https://doi.org/10.5194/gmd-12-4627-2019, 2019.

Saad, K. M., Wunch, D., Toon, G. C., Bernath, P., Boone, C., Connor, B., Deutscher, N. M., Griffith, D. W. T., Kivi, R., Notholt, J., Roehl, C., Schneider, M., Sherlock, V., and Wennberg, P. O.: Derivation of tropospheric methane from TCCON CH_4 and HF total column observations, Atmos. Meas. Tech., 7, 2907–2918, https://doi.org/10.5194/amt-7-2907-2014, 2014.

Sargent, M., Barrera, Y., Nehrkorn, T., Hutyra, L. R., Gately, C. K., Jones, T., McKain, K., Sweeney, C., Hegarty, J., Hardiman, B., Wang J. A., and Wofsy, S. C.: Anthropogenic and biogenic CO_2 fluxes in the Boston urban region, P. Natl. Acad. Sci. USA, 115, 7491–7496, https://doi.org/10.1073/pnas.1803715115, 2018.

Shekhar, A., Chen, J., Paetzold, J. C., Dietrich, F., Zhao, X., Bhattacharjee, S., Ruisinger, V., and Wofsy, S. C.: Anthropogenic CO_2 emissions assessment of Nile Delta using XCO_2 and SIF

data from OCO-2 satellite, Environ. Res. Lett., 15, 095010, https://doi.org/10.1088/1748-9326/ab9cfe, 2020.

Skamarock, W., Klemp, J., Dudhia, J., Gill, D., Barker, D., Duda, M., Huang, X., Wang, W., and Powers, J.: Description of the Advanced Research WRF Version 3, Tech. rep., National Center for Atmospheric Research, https://pdfs.semanticscholar.org/ace5/4d4d1d6c9914997ad8f4e410044fdeb95b9d.pdf (last access: 10 September 2023), 2008.

Staufer, J., Broquet, G., Bréon, F.-M., Puygrenier, V., Chevallier, F., Xueref-Rémy, I., Dieudonné, E., Lopez, M., Schmidt, M., Ramonet, M., Perrussel, O., Lac, C., Wu, L., and Ciais, P.: The first 1-year-long estimate of the Paris region fossil fuel CO_2 emissions based on atmospheric inversion, Atmos. Chem. Phys., 16, 14703–14726, https://doi.org/10.5194/acp-16-14703-2016, 2016.

Super, I., Denier van der Gon, H. A. C., van der Molen, M. K., Sterk, H. A. M., Hensen, A., and Peters, W.: A multi-model approach to monitor emissions of CO_2 and CO from an urban–industrial complex, Atmos. Chem. Phys., 17, 13297–13316, https://doi.org/10.5194/acp-17-13297-2017, 2017.

Super, I., Dellaert, S. N. C., Visschedijk, A. J. H., and Denier van der Gon, H. A. C.: Uncertainty analysis of a European high-resolution emission inventory of CO_2 and CO to support inverse modelling and network design, Atmos. Chem. Phys., 20, 1795–1816, https://doi.org/10.5194/acp-20-1795-2020, 2020.

Toja-Silva, F., Chen, J., Hachinger, S., and Hase, F.: CFD simulation of CO_2 dispersion from urban thermal power plant: Analysis of turbulent Schmidt number and comparison with Gaussian plume model and measurements, J. Wind Eng. Ind. Aerod., 169, 177–193, https://doi.org/10.1016/j.jweia.2017.07.015, 2017.

Tu, Q., Hase, F., Blumenstock, T., Kivi, R., Heikkinen, P., Sha, M. K., Raffalski, U., Landgraf, J., Lorente, A., Borsdorff, T., Chen, H., Dietrich, F., and Chen, J.: Intercomparison of atmospheric CO_2 and CH_4 abundances on regional scales in boreal areas using Copernicus Atmosphere Monitoring Service (CAMS) analysis, COllaborative Carbon Column Observing Network (COCCON) spectrometers, and Sentinel-5 Precursor satellite observations, Atmos. Meas. Tech., 13, 4751–4771, https://doi.org/10.5194/amt-13-4751-2020, 2020.

Turner, A. J., Shusterman, A. A., McDonald, B. C., Teige, V., Harley, R. A., and Cohen, R. C.: Network design for quantifying urban CO_2 emissions: assessing trade-offs between precision and network density, Atmos. Chem. Phys., 16, 13465–13475, https://doi.org/10.5194/acp-16-13465-2016, 2016.

USEPA: Global Non-CO_2 Greenhouse Gas Emission Projections Mitigation Potential: 2015–2050, Tech. rep., US Environmental Protection Agency Washington, DC, ePA-430-R-19-010, https://www.epa.gov/global-mitigation-non-co2-greenhouse-gases/global-non-co2-greenhouse-gas-emission-projections (last access: 10 September 2023), 2019.

van der Gon, H. D., Kuenen, J., Boleti, E., Muntean, M., Greet, M., Marshall, J., and Haussaire, J.-M.: Emissions and natural fluxes Dataset, Tech. rep., The CO_2 Human Emissions Project (CHE) Consortium, https://www.che-project.eu/node/149 (last access: 10 September 2023), 2019.

Vaughn, T. L., Bell, C. S., Pickering, C. K., Schwietzke, S., Heath, G. A., Pétron, G., Zimmerle, D. J., Schnell, R. C., and Nummedal, D.: Temporal variability largely explains top-down/bottom-up difference in methane emission estimates from a natural gas production region, P. Natl. Acad. Sci. USA, 115, 11712–11717, https://doi.org/10.1073/pnas.1805687115, 2018.

Vermote, E.: MOD09A1 MODIS Surface Reflectance 8-Day L3 Global 500m SIN Grid V006, United States Geological Survey, https://doi.org/10.5067/MODIS/MOD09A1.006, 2015.

Viatte, C., Lauvaux, T., Hedelius, J. K., Parker, H., Chen, J., Jones, T., Franklin, J. E., Deng, A. J., Gaudet, B., Verhulst, K., Duren, R., Wunch, D., Roehl, C., Dubey, M. K., Wofsy, S., and Wennberg, P. O.: Methane emissions from dairies in the Los Angeles Basin, Atmos. Chem. Phys., 17, 7509–7528, https://doi.org/10.5194/acp-17-7509-2017, 2017.

Vogel, F. R., Frey, M., Staufer, J., Hase, F., Broquet, G., Xueref-Remy, I., Chevallier, F., Ciais, P., Sha, M. K., Chelin, P., Jeseck, P., Janssen, C., Té, Y., Groß, J., Blumenstock, T., Tu, Q., and Orphal, J.: XCO_2 in an emission hot-spot region: the COCCON Paris campaign 2015, Atmos. Chem. Phys., 19, 3271–3285, https://doi.org/10.5194/acp-19-3271-2019, 2019.

Wei, T., Wu, J., and Chen, S.: Keeping track of greenhouse gas emission reduction progress and targets in 167 cities worldwide, Front. Sustain. Cities, 3, p. 64, https://doi.org/10.3389/frsc.2021.696381, 2021.

Wu, D., Lin, J. C., Fasoli, B., Oda, T., Ye, X., Lauvaux, T., Yang, E. G., and Kort, E. A.: A Lagrangian approach towards extracting signals of urban CO_2 emissions from satellite observations of atmospheric column CO_2 (XCO_2): X-Stochastic Time-Inverted Lagrangian Transport model ("X-STILT v1"), Geosci. Model Dev., 11, 4843–4871, https://doi.org/10.5194/gmd-11-4843-2018, 2018.

Wunch, D., Toon, G. C., Sherlock, V., Deutscher, N. M., Liu, C., Feist, D. G., and Wennberg, P. O.: Documentation for the 2014 TCCON Data Release, CaltechDATA [data set], https://doi.org/10.14291/TCCON.GGG2014.DOCUMENTATION.R0/1221662, 2015.

Zhao, X., Marshall, J., Hachinger, S., Gerbig, C., Frey, M., Hase, F., and Chen, J.: Analysis of total column CO_2 and CH_4 measurements in Berlin with WRF-GHG, Atmos. Chem. Phys., 19, 11279–11302, https://doi.org/10.5194/acp-19-11279-2019, 2019.